

Landau-Zener without a Qubit: Unveiling Multiphoton Interference, Synthetic Floquet Dimensions, and Dissipative Quantum Chaos

Léo Peyruchat,^{1,2} Fabrizio Minganti,^{2,3} Marco Scigliuzzo,^{2,4} Filippo Ferrari,^{2,3}
Vincent Jouanny,^{1,2} Franco Nori,^{5,6,7} Vincenzo Savona,^{2,3} and Pasquale Scarlino^{1,2,*}

¹Hybrid Quantum Circuits Laboratory (HQC), Institute of Physics,
École Polytechnique Fédérale de Lausanne (EPFL), 1015 Lausanne, Switzerland

²Center for Quantum Science and Engineering,
École Polytechnique Fédérale de Lausanne (EPFL), CH-1015 Lausanne, Switzerland

³Laboratory of Theoretical Physics of Nanosystems (LTPN), Institute of Physics,
École Polytechnique Fédérale de Lausanne (EPFL), 1015 Lausanne, Switzerland

⁴Laboratory of Photonics and Quantum Measurements (LPQM),
Institute of Physics, EPFL, CH-1015 Lausanne, Switzerland

⁵Theoretical Quantum Physics Laboratory, Cluster for Pioneering Research, RIKEN, Wako-shi, Saitama 351-0198, Japan

⁶Quantum Information Physics Theory Research Team,
Quantum Computing Center, RIKEN, Wakoshi, Saitama, 351-0198, Japan

⁷Physics Department, The University of Michigan, Ann Arbor, Michigan 48109-1040, USA
(Dated: April 17, 2024)

Landau-Zener-Stückelberg-Majorana (LZSM) interference emerges when the parameters of a *qubit* are periodically modulated across an avoided level crossing. Here, we investigate the occurrence of the LZSM phenomenon in nonlinear multilevel bosonic systems, where the interference pattern is determined by multiple energy levels and cannot be described by a level crossing between only two states. We fabricate two superconducting resonators made of flux-tunable Josephson junction arrays. The first device is very weakly nonlinear (the nonlinearity is smaller than the photon-loss rate) and, when a weak driving field is applied, it behaves as a linear resonator, yet shows the same LZSM interference as in a two-level system. Notably, here the interference originates from multiple avoided level crossings of the harmonic ladder. When subjected to a stronger drive, nonlinear effects start playing a role, and the interference pattern departs from the one observed in two-level systems. We demonstrate that, when two or more LZSM interference peaks merge, dissipative quantum chaos emerges. In the second device, where the nonlinearity surpasses the photon-loss rate, we observe additional LZSM interference peaks due to Kerr multiphoton resonances. When described under the light of the Floquet theory, these resonances can be interpreted as synthetic modes of an array of coupled cavities. We derive a simple effective model highlighting the essential features of the entirety of these phenomena. As the control of LZSM in qubit systems led to the implementation of fast protocols for characterization and state preparation, our findings pave the way to better control of nonlinear resonators, with implications for diverse quantum technological platforms.

I. INTRODUCTION

Qubits – two-level systems – are the building blocks of digital quantum computers and simulators, as well as an essential paradigm for describing many quantum systems [1, 2]. Understanding and controlling their dynamics is thus pivotal to the progress of quantum technologies. When the qubit’s energy-level splitting is varied in such a way that the two levels become almost degenerate, the Landau-Zener-Stückelberg-Majorana (LZSM) [3–6] transition probability dictates the likelihood of non-adiabatic transitions between the ground and excited states. When the variation of the splitting is periodic in time, a rich *LZSM interference pattern* arises, as schematically shown in Fig. 1 (a) (see Ref. [7] for a recent overview of the field). At each oscillation period, the transition paths can interfere constructively or destructively to determine the final probability of the qubit

to reach the excited state, as observed in, e.g., superconducting qubit architectures [8, 9], semiconductor quantum dots [10, 11], and nitrogen-vacancy center in diamond [12].

Historically, the understanding of LZSM transitions was a foundational step in the development of non-relativistic quantum mechanics [3–6]. Recently, LZSM interference gained also considerable attention, as a versatile tool for the study of quantum systems. Examples include the characterization of the frequency noise of superconducting resonators [13] and the decoherence properties of charge states from steady-state measurements [11, 14, 15]. LZSM interferometry was also employed for the fast coherent control of charge qubits [16, 17], and to mediate and control the coupling of a qubit to multiple mechanical modes [18]. Finally, LZSM interferometry has also been proposed as a tool for the preparation of exotic quantum states, such as two-level systems with tunable absorption properties [19], correlated photons [20] and Schrödinger-cat states [21, 22]. The physics of LZSM interference beyond the two-level approximation has been marginally investi-

* E-mail: pasquale.scarlino@epfl.ch

gated, and often focuses on isolated avoided level crossing within a larger multilevel structure [7]. Furthermore, coupled classical oscillators have been proposed [23] and studied [24, 25] as classical systems displaying LZSM interferences. Indeed, in the presence of tailored modulation, these *multimode classical systems* display the same equation of motion of a qubit [26], and thus exhibit LZSM interference due to the presence of an effective two-level system.

In bosonic systems, the qubit limit can be reached by the introduction of a Kerr nonlinearity (anharmonicity) χ , permitting, in principle, to address only the ground and first excited states [1]. This description applies to several platforms, including superconducting circuits [27], polaritonic microcavities [28], mechanical resonators [29], and the vibration of trapped ions [30]. A realistic description of these systems must include the effects of dissipative processes, which blur the distinction between energy levels and thus hinder the possibility of addressing them singularly. Depending on the magnitude of the total loss rate κ , one can thus determine two distinct regimes that we dub the Kerr ($|\chi| > \kappa$) and Duffing ($|\chi| < \kappa$) regimes [31]. In the Kerr regime, depicted in Fig. 1 (b), the energy quantization of the bosonic mode is still accessible despite the presence of dissipation [32]. The system can absorb n photons from a drive and transition to the n th excited level, in a process known as *Kerr multiphoton resonance* (or multiphoton transition) [33]. In the Duffing regime [Fig. 1(c)], instead, dissipation blurs these multiphoton resonances, giving rise to a single spectral feature, where the energy quantization of the underlying boson can't be resolved. The effect of the nonlinearity, in this case, is to shift this resonance, leading to phenomena such as bistability and hysteresis [34–36]. Multimodal Duffing oscillators, where multiple bistabilities are present, display emergent phenomena, such as the formation of domain walls and dissipative phase transitions [37–39], as well as dissipative quantum chaos [40]. The latter is triggered by the combined presence of classical and quantum fluctuations and the competition of unitary dynamics and dissipative processes [41, 42].

In this article, we discover a new paradigm of LZSM physics, through the study of two nonlinear superconducting resonators, one in the Kerr and one in the Duffing regime. Given the high degree of tunability of the drive, the modulation, and the other system parameters, we determine the whole LZSM interference diagram for nonlinear bosonic systems. We present a simple unified model that captures the relevant features of the system under consideration.

The main results of this work can be summarized as follows.

First, we experimentally demonstrate and theoretically clarify that, at low driving amplitude, the LZSM interference pattern is independent of the nonlinearity of the system [c.f. the rightmost panels of Figs. 1(a) and (d)]. Namely, there is no distinction in the LZSM interfer-

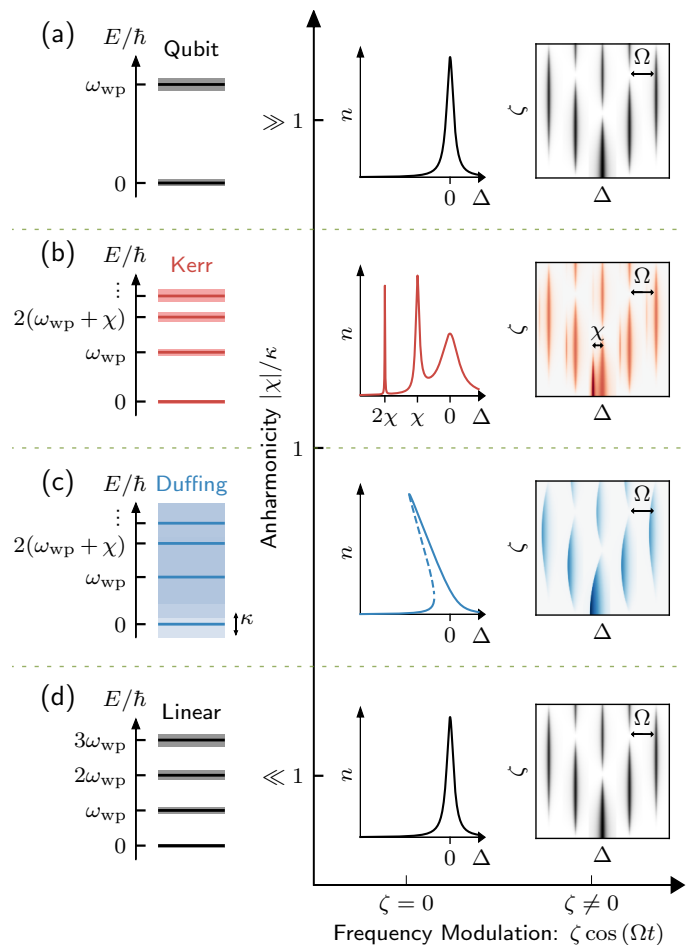


FIG. 1. Landau-Zener-Stückelberg-Majorana (LZSM) interference mechanisms in bosonic systems. For cases studied in this article, we show the level structure of the undriven system (left); the photon number n of the driven, but not-modulated, system as a function of the pump-to-cavity detuning Δ (center); and the LZSM pattern emerging when the cavity eigenfrequency is periodically modulated with strength ζ and frequency Ω (right). (a) In the qubit regime of infinite nonlinearity, the system consists only of the ground and excited states. This level structure gives rise to a single excitation peak ($|0\rangle \rightarrow |1\rangle$) at detuning $\Delta = 0$. Thus, the standard LZSM interference pattern emerges. (b) In the Kerr regime, where the anharmonicity is larger than the loss ($|\chi| > \kappa$), the system consists of many uneven-spaced states with different numbers of excitations. When $\Delta = n\chi$, multiphoton transitions $|0\rangle \rightarrow |n\rangle$ occur for large-enough drive. This multiphotonic transition structure is periodically repeated around each standard LZSM peak. (c) In the Duffing regime, where the anharmonicity is smaller than the loss ($|\chi| < \kappa$), the uneven-spaced states are broadened by dissipation and cannot be distinguished. The drive excites multiple levels, resulting in a deviation from a Lorentzian shape, and the Kerr nonlinearity competes with detuning, giving rise to bistability. Such a deviation and the presence of bistability are imprinted in each LZSM peak. (d) In the linear regime ($\chi = 0$), all levels are equispaced. When driven, only a Lorentzian peak appears at $\Delta = 0$, similar to the qubit regime. Upon modulation of the resonator frequency, the LZSM interference is also indistinguishable from that in the qubit regime.

ence pattern between a completely linear resonator and a qubit.

Second, we show novel effects due to the competition between the modulation and the nonlinearity at larger pumping power, demonstrating the role of dissipation [Figs. 1 (b) and (c)]. In particular (i) In the Kerr regime, we observe how Kerr multiphoton resonances add structure to the LZSM interference. These resonances and the associated quasi-energy (Floquet) states can be interpreted as the modes of a multimode synthetic cavity array, with effective interference between these multiple transitions resulting in avoided level crossings. (ii) In the Duffing regime, we show how bistability and hysteresis come into play in determining the state of the system, suggesting the emergence of dissipative quantum chaos in a Floquet regime, i.e., Floquet-dissipative quantum chaos.

Our work establishes a comprehensive framework for understanding LZSM and Floquet physics, clarifying the role of nonlinearity and dissipation in determining the interference patterns. It paves the way to their control, with perspectives for *synthetic dimension engineering* in Floquet configurations. This platform can be used as a quantum simulator to investigate quantum chaos and critical phenomena in highly controllable superconducting systems.

The article is organized as follows. In Sec. II we characterize the devices and provide a model describing them. We then investigate LZSM interference in the qubit and linear regimes in Sec. III. In Sec. IV we study LZSM interference beyond the standard qubit regime. In particular, in Sec. IV A we investigate the Kerr regime, where multiphoton resonances participate in determining the emergent LZSM interference. In Sec. IV B, instead, we study the system in the Duffing regime and show the emergence of Floquet dissipative quantum chaos. We draw our conclusions in Sec. V. The appendices are devoted to the details on the theoretical derivation of the effective model as well as the numerical methods used to study the system (Appendix A), the description of the experimental setup and the calibration of the experiment (Appendix B), and additional measurements (Appendix C).

II. EXPERIMENTAL SYSTEM AND MODEL

We aim to investigate all regimes of nonlinearity and dissipation, namely, qubit, Kerr, Duffing, and linear, as shown in Figs. 1 (a-d), respectively. To this extent, we design and fabricate two frequency-tunable nonlinear resonators that can operate in these different regimes according to the driving amplitude. These are superconducting SQUID arrays [43–45], galvanically connected to ground on one side, and capacitively shunted to the ground on the other side, as shown in Figs. 2 (a), (b), and (f). A detailed summary of their parameters is reported in Table I.

The frequency of the resonators can be tuned by a dedicated flux line that uniformly threads the magnetic fields in each SQUID loop (in purple) and an external superconducting coil. The two resonators differ in the number of SQUIDs in each array, as highlighted by red and blue false colors, determining the two orders of magnitude difference in their Kerr nonlinearity χ . Hereafter, the red and blue color schemes will always indicate measurements of the devices in the **Kerr/qubit** and **Duffing/linear** regimes, respectively. Each resonator is also capacitively coupled to a feedline (in green) in a notch configuration, resulting in an external coupling κ_{ext} close to the internal dissipation rate κ_{int} (critically coupled regime). We define the total dissipation rate as $\kappa = \kappa_{\text{ext}} + \kappa_{\text{int}}$.

Each device is thermally and mechanically anchored at the mixing chamber plate of a dilution refrigerator, reaching an average base temperature of 15 mK. The devices are probed by a coherent drive with amplitude F at the sample, injected in the feedline through highly attenuated coaxial lines. The drive amplitude is related to the input power P_{in} by $F = \sqrt{P_{\text{in}}\kappa_{\text{ext}}/\hbar\omega_{\text{d}}}$, where ω_{d} is the drive frequency. Although the frequency of the untuned cavity is ω_{c} , through the paper, the frequency working point of the resonators, ω_{wp} , is set by a static flux generated by direct current through an external superconducting coil. The flux operating point is $\Phi_{\text{wp}} = 0.45\Phi_0$ for the $N = 10$ device, while $\Phi_{\text{wp}} = 0.32\Phi_0$ for the $N = 32$ one, where $\Phi_0 = h/2e$ is the magnetic flux quantum. Finally, driving the fluxline at a frequency Ω periodically modulates the frequency of the resonator, approximately between $\omega_{\text{wp}} \pm \zeta$, with ζ representing the strength of the modulation. The single-tone spectroscopy of the resonators at low-driving power as a function of the external magnetic flux is reported in Appendix B.

Both devices can be modeled as a bosonic mode with the following time-dependent Hamiltonian:

$$\hat{H}/\hbar = -\Delta\hat{a}^\dagger\hat{a} + \chi\hat{a}^\dagger\hat{a}^\dagger\hat{a}\hat{a} + F(\hat{a} + \hat{a}^\dagger) + \zeta\cos(\Omega t)\hat{a}^\dagger\hat{a}, \quad (1)$$

where $\Delta = \omega_{\text{d}} - \omega_{\text{wp}}$ is the detuning between the working point of the devices (ω_{wp}) and the drive frequency (ω_{d}). Beyond the total dissipation rate κ , the system is subject to dephasing with rate κ_ϕ . We include them in the time evolution of the density matrix $\hat{\rho}$ using the Lindblad master equation

$$\hbar\partial_t\hat{\rho} = -i\left[\hat{H}, \hat{\rho}\right] + \kappa\mathcal{D}[\hat{a}]\hat{\rho} + \kappa_\phi\mathcal{D}[\hat{a}^\dagger\hat{a}]\hat{\rho}. \quad (2)$$

Here, $\mathcal{D}[\hat{L}]\hat{\rho} \equiv \hat{L}\hat{\rho}\hat{L}^\dagger - \{\hat{L}^\dagger\hat{L}, \hat{\rho}\}/2$ is the Lindblad dissipator [46].

In Fig. 2 we characterize the coherent response of the resonators in the absence of modulation (i.e., $\zeta = 0$) and use it to determine the parameters of the two devices. In Figs. 2 (c) and (d) we report the magnitude and phase of the transmission coefficient S_{21} (see Appendix B 3) as a function of the driving power $P_{\text{in}} \propto F^2$ in the Kerr regime. At low power, only a single dip around $\Delta = 0$ is visible, representing the transition to the first excited

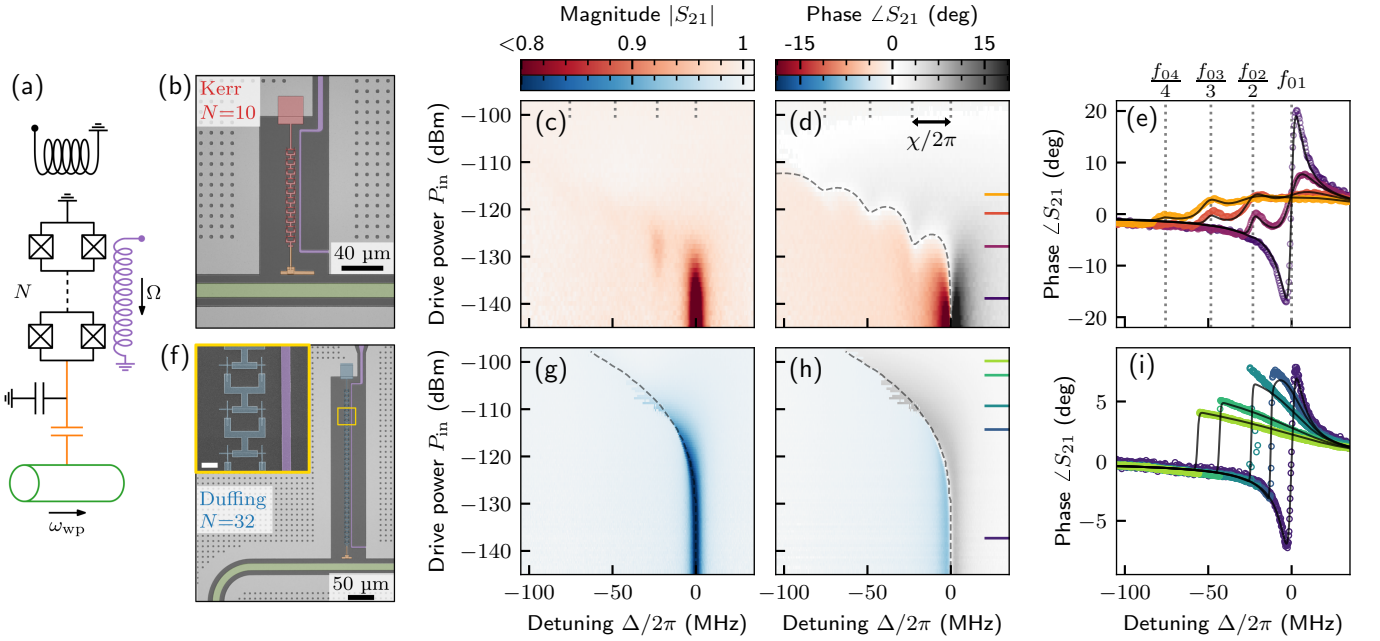


FIG. 2. SQUID array characterization. (a) Equivalent lumped electrical circuit of the device composed of N SQUIDs in series. The static flux is controlled via an external coil and a microwave signal can be applied to the flux line (purple) for fast frequency modulation. The resonator is coupled to a feedline in a notch configuration. (b, f) Optical micrograph of the two SQUID array resonators studied in this work with $N = 10$ (red) and $N = 32$ (blue) SQUIDs, with details on the Josephson junction shown in the inset where the white scale bar represents $5\ \mu\text{m}$. (c-d) For the Kerr case ($N = 10$), the magnitude and phase of the transmission coefficient through the feedline as a function of drive power at the sample. The black dashed curve indicates where the phase of S_{21} is zero according to numerical simulations, highlighting the position of the multiphoton resonances. (e) Selected traces of the data reported in panel (d). Experimental data are shown with circle markers whose colors correspond to the ticks in panel (d). Numerical fits to a full quantum model are shown in black solid lines. The grey dotted vertical lines indicate the position of the multiphoton resonances obtained from numerical simulations. (g-i) Same measurement as in (c-e), but for the Duffing case. The dashed curves in (g,h) indicate the minima of $|S_{21}|$ obtained from a full quantum simulation. Additional details on the characterization of the two devices are given in Appendix B.3.

TABLE I. Summary of the relevant SQUID array parameters at flux operating point Φ_{wp} .

| Parameters | $N = 10$ device (Kerr/Qubit regime) | $N = 32$ device (Duffing/Linear regime) | Description |
|----------------------------|--|--|----------------------------------|
| $ \chi /\kappa$ | 5 | 0.05 | Photon-number distinguishability |
| $\omega_c/2\pi$ | ≈ 13 GHz | ≈ 6.4 GHz | Zero-flux frequency |
| $\omega_{\text{wp}}/2\pi$ | 4.502 GHz | 4.306 GHz | Frequency at Φ_{wp} |
| Φ_{wp}/Φ_0 | 0.45 | 0.32 | Flux operating point |
| $\chi/2\pi$ | -23.5 MHz | -0.35 MHz | Kerr nonlinearity |
| $\kappa_{\text{in}}/2\pi$ | 1.1 MHz | 4.92 MHz | Internal loss rate |
| $\kappa_{\text{ext}}/2\pi$ | 3.75 MHz | 1.49 MHz | External loss rate |
| $\kappa/2\pi$ | 4.85 MHz | 6.41 MHz | Total loss rate |
| $\kappa_\phi/2\pi$ | 0.75 MHz | 0.4 MHz | Dephasing rate |

state (noted as $|0\rangle \rightarrow |1\rangle$, where $|n\rangle$ is the photon number state of the resonator). At larger values of the drive, several dips appear, representing the so-called Kerr multiphoton transitions between the ground state and the higher-excited levels ($|0\rangle \rightarrow |n\rangle$), highlighted in the single traces shown in Fig. 2 (e). According to Eq. (1), all the dips should appear at $\Delta \simeq (n-1)\chi$. Small deviations from this prediction are due to higher-order nonlinearities [47]. For even larger powers, the nonlinearity suppresses

the intracavity photon number with respect to the input power, resulting in an almost unitary transmission S_{21} .

We report the same measurements for the resonator in the Duffing regime in Figs. 2 (g-i). In this case, dissipation smears the multiphoton resonances, resulting in an indistinguishable level structure. Increasing the drive, the single dip of S_{21} originally at $\Delta = 0$ moves to negative detunings, indicating that the drive is exciting higher levels. Scanning the detuning from negative to positive val-

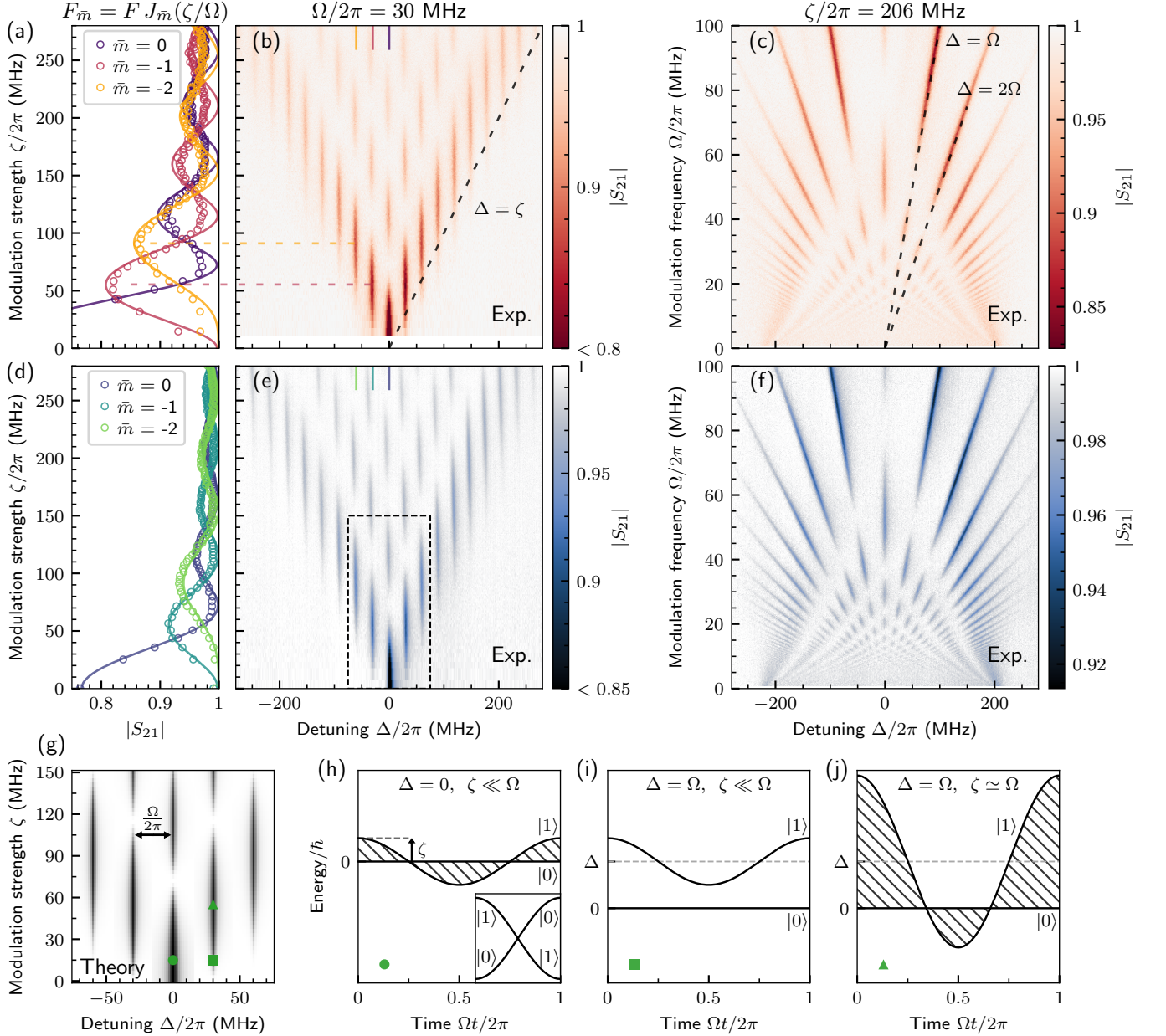


FIG. 3. LZSM interference patterns. (a-c, red) Analysis of the $N = 10$ device, with input power $P_{\text{in}} = -138.8$ dBm, ensuring that we are in the *qubit regime*. (b) The transmission coefficient $|S_{21}|$ as a function of the detuning Δ and the modulation strength ζ , for fixed modulation frequency $\Omega/2\pi = 30$ MHz [see Eq. (1)]. (a) Comparison of the experimental and theoretical data for $|S_{21}|$. Solid lines represent the results of the numerical simulations of the full quantum model obtained at $\Delta = 0$, $\Delta = -\Omega$, and $\Delta = -2\Omega$ (see A 1 a). The circles are the experimental data obtained from panel (b), in which Δ is slightly re-scaled to account for the nonlinear flux-dependency of the resonator frequency (see Appendix B). (c) $|S_{21}|$ as a function of Δ and Ω . (d-f, blue) As in (a-c), but for the $N = 32$ device, with $P_{\text{in}} = -133.3$ dBm to ensure that the system is in the *linear regime*. From these plots, the two regimes appear almost indistinguishable. (g) The photon number versus Δ and ζ is obtained from a simulation using the effective model of Eq. (3) that reproduces the interference pattern in panels (b) and (e). (h-j) Depiction of the time evolution of the energy level $|1\rangle$, in the frame rotating at the drive frequency ω_d , if $F = 0$. A finite drive F opens gaps at each crossing between $|0\rangle$ and $|1\rangle$, allowing a non-adiabatic passage between the two. The parameters Δ and ζ are indicated by green markers in (g). (h) At $\Delta = 0$, the level $|1\rangle$ becomes resonant with $|0\rangle$ (they form a level crossing, see the inset). The values of ζ , F , and κ then determine the probability of transitioning out of the vacuum. (i) For non-zero detuning (e.g. $|\Delta| = \Omega$) and small modulation ($\zeta \ll \Omega$), the level $|1\rangle$ is never resonant with $|0\rangle$ and it cannot be populated. (j) For strong enough modulation $\zeta > |\Delta|$, the level $|1\rangle$ can form again an avoided level crossing, and constructive interference is possible again.

ues, as done in Fig. 2 (i), reveals the presence of a sharp jump, where the resonator passes from a highly- to a

lowly-populated phase. This behavior is associated with optical bistability, i.e., the presence of two metastable states that require a long time to decay to the steady state [37, 38]. This phenomenon gives rise to hysteresis [35, 36] and makes it difficult to properly resolve the exact detuning where the transition occurs.

III. LINEAR AND QUBIT LZSM INTERFERENCE

We can investigate the linear and qubit regimes using the $N = 10$ and $N = 32$ resonators described above. Indeed, for the $N = 10$ resonator, the second-excited level is not significantly populated if $F^2 \ll |\chi|\kappa$ [48]. For the $N = 10$ device parameters and the drive $F/2\pi \simeq 1.6$ MHz considered here, the third level is predicted to be populated less than 0.03%. For the values used in this first part of the experiment, the system effectively behaves like an ideal qubit subject to dissipation and dephasing. We report the experimental data in Figs. 3 (b) and (c). In Fig. 3 (b) we show the norm of the scattering coefficient S_{21} sweeping the detuning Δ , for a fixed modulation frequency Ω , and varying the modulation strength ζ . One observes the LZSM pattern emerging, with populated regions at $\Delta = m\Omega$, for integer m . Fixing ζ and scanning Ω , in Fig. 3 (c) we observe again the interference pattern at $\Delta = m\Omega$. We thus confirm the presence of LZSM interference and the control over the modulation of the resonator in the Kerr regime.

We now consider the $N = 32$ device. In this case, the oscillator approximately behaves as a purely linear resonator if $F < \sqrt{\kappa^3/|\chi|}$ [49]. For the $N = 32$ device parameters and the drive $F/2\pi \simeq 3$ MHz considered here, we estimate a relative photon-number deviation from a completely linear resonator of less than 3%. Within this regime, we repeat the previous measurements and report them in Figs. 3 (e) and (f). Surprisingly, we observe the same interference pattern emerging, with *no distinguishable differences between the qubit and the completely linear case*.

This feature indicates that only the energy difference between $|0\rangle$ and $|1\rangle$ determines the interference pattern in both the qubit and the linear regimes [c.f. Figs. 3 (g-j)]. To provide a more quantitative reasoning, we choose \bar{m} minimizing $\Delta - \bar{m}\Omega$ and, following the procedure derived in Appendix A 3, and passing in the frame rotating at the frequency $\bar{m}\Omega$, we have

$$\hat{H}_{\bar{m}}/\hbar \simeq -\Delta_{\bar{m}}\hat{a}^\dagger\hat{a} + \chi\hat{a}^\dagger\hat{a}^\dagger\hat{a}\hat{a} + F_{\bar{m}}(\hat{a} + \hat{a}^\dagger), \quad (3)$$

where the renormalized detuning $\Delta_{\bar{m}}$ and renormalized drive $F_{\bar{m}}$ are

$$\Delta_{\bar{m}} = (\Delta - \bar{m}\Omega), \quad F_{\bar{m}} = FJ_{\bar{m}}\left(\frac{\zeta}{\Omega}\right), \quad (4)$$

with $J_{\bar{m}}(\zeta/\Omega)$ indicating the Bessel function of the first kind. All dissipative terms maintain their form as in

Eq. (2). In other words, when we can single out a single relevant frequency $\Delta_{\bar{m}}$ for each of the LZSM interference dips, the devices behave as a collection of independent nonlinear resonators, whose driving amplitudes $F_{\bar{m}}$ are unmodulated via Bessel functions. For the parameters we consider here, and if we also assume a weak enough drive to be in the linear and qubit regime [48, 49], we obtain

$$\langle \hat{a}^\dagger \hat{a} \rangle \simeq \frac{4F_{\bar{m}}^2}{\kappa} \frac{\kappa + \beta\kappa_\phi}{4\Delta_{\bar{m}}^2 + (\kappa + \beta\kappa_\phi)^2}, \quad (5)$$

with $\beta = 1$ for a linear resonator regime and $\beta = 4$ in the weakly driven qubit limit. Namely, the *two regimes have identical interference patterns*, only slightly modulated by the dephasing rate κ_ϕ . To further demonstrate the validity of these results, additional LZSM interference patterns are reported in Appendix C, highlighting the precise control of the number and frequency spacing of modes over a broad range of modulation strengths and frequencies.

The approximation of the effective model correctly captures the value of the photon number, but not that of the field \hat{a} (and thus cannot be used to quantitatively study S_{21}). As is discussed in Appendix A 3, to correctly capture this feature, one has to resort to a full quantum simulation of the Floquet model (see Appendix A 1 a). This is shown in Figs. 3 (a) and (d), where we plot $|S_{21}|$ of the first three LZSM lobes, comparing the experimental data with the theoretical predictions both for the qubit and linear regimes. In both cases, we find an *excellent agreement between theory and experiments*. We note that the maxima and the minima of $|S_{21}|$ of the \bar{m} th LZSM mode coincides with the extremes of the associated Bessel function $J_{\bar{m}}$, showing the qualitative validity of Eq. (3) in describing also S_{21} .

We remark here that the Hamiltonian in Eq. (3) could be obtained approximating the response of an array of nonlinear resonators, each at a frequency $\Delta_{\bar{m}}$. Therefore, we can mathematically interpret each of the LZSM dips as the response of a different *Floquet synthetic mode*. As we show below, by increasing the drive, these initially non-interacting modes will begin to interact.

IV. LZSM BEYOND THE QUBIT APPROXIMATION

We now focus on those phenomena emerging due to the simultaneous presence of the multilevel structure of the nonlinear resonators and the modulation of their eigenenergies, studying the devices beyond their qubit and linear regimes.

A. Kerr regime

In the Kerr regime and for strong enough drives to probe the multiphoton transitions [48], we investigate

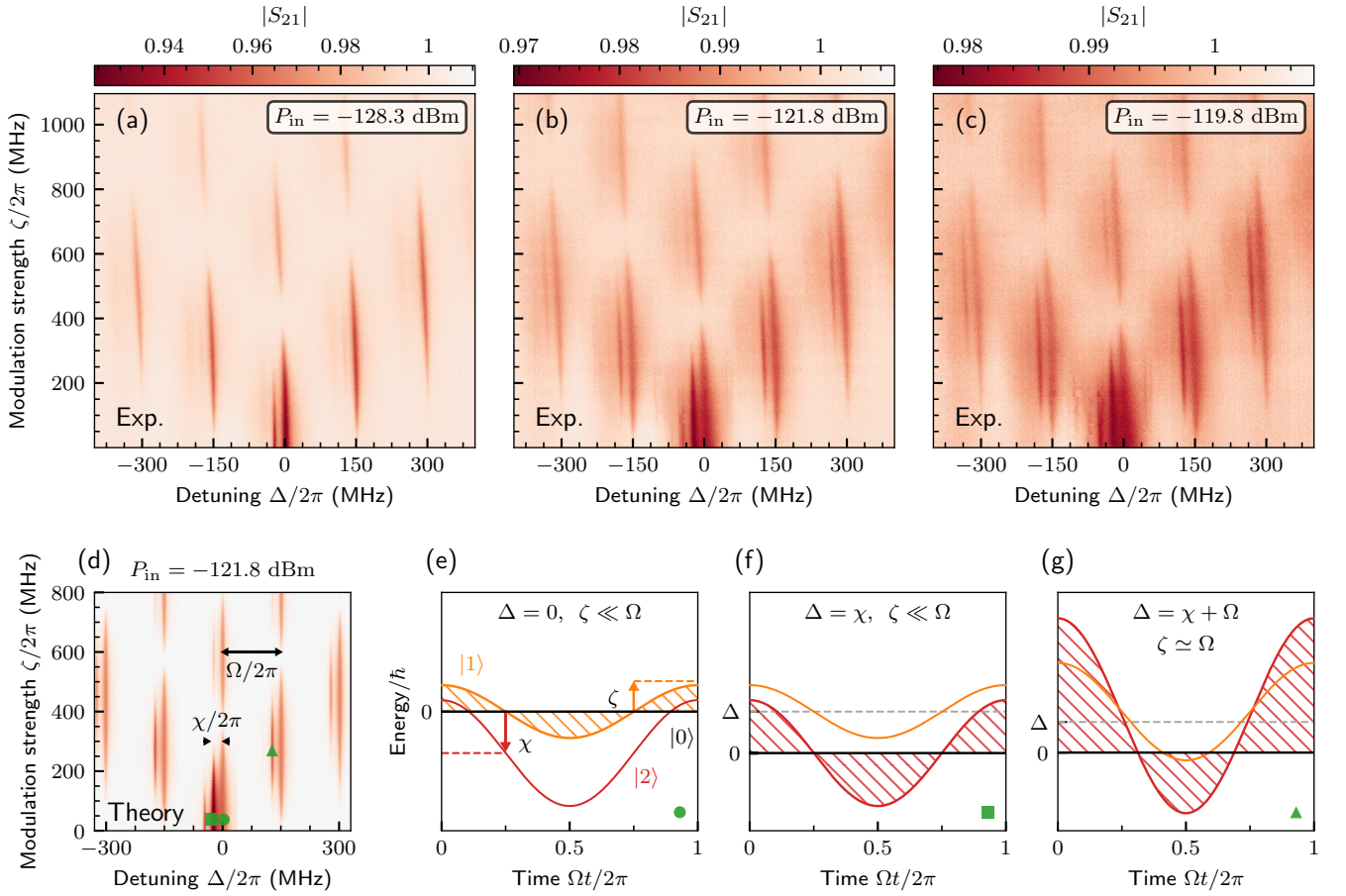


FIG. 4. LZSM interferometry for the $N = 10$ device, in the Kerr regime and strongly-modulated case $\Omega \gg |\chi|$. (a-c) The magnitude of S_{21} is measured versus Δ and ζ for fixed modulation frequency $\Omega/2\pi = 150$ MHz. As the drive power P_{in} is increased, Kerr multiphoton resonances from $|0\rangle$ to $|n\rangle$ appear detuned by $(n-1)\chi$ on the left of bare LZSM resonances. For large ζ , notice the shift of the pattern to negative detuning, due to the nonlinear dependence of the SQUID array frequency on the flux, as explained in Appendix B. (d) Photon-number simulation using the effective model of Eq. (3) for the same parameters as in panel (b), recovering the same interference pattern. (e-g) In the drive frame, energy versus time for different values of ζ and Δ including the first three levels of an undriven Kerr resonator ($F = 0$). Green markers indicate the corresponding value of Δ and ζ in (d). (e) For $\Delta = 0$, although multiple levels cross with $|0\rangle$, only the level $|1\rangle$ form a constructive interference. (f) For $\Delta = \chi$, the second level $|2\rangle$ crosses $|0\rangle$, and an appropriate choice of parameters leads to constructive interference. (g) For $\Delta = \chi + \Omega$, similar LZSM interference can be constructive again and the level $|2\rangle$ can be populated. We verified that both the data and full numerical simulations recover that the interference patterns are fully constructive at $\Delta = \Omega$ and $\zeta \approx 1.84\Omega$, where the Bessel function $J_1(\zeta/\Omega)$ is at a maximum, confirming the prediction of the effective model in Eq. (3).

how the frequency and amplitude of the modulation modifies the multiphoton resonances.

The system's behavior around the multiphoton resonance $|0\rangle \rightarrow |n\rangle$ occurring for $\Delta \simeq \chi(n-1)$ can be described by a 2×2 matrix. For instance, the $|0\rangle \rightarrow |2\rangle$ multiphoton transition can be described as

$$\hat{H}^{(2)}/\hbar = 2[-\Delta + \chi + \zeta \cos(\Omega t)] |2\rangle\langle 2| + G^{(2)}(|0\rangle\langle 2| + \text{h.c.}), \quad (6)$$

where $G^{(2)}$ represents the effective drive between the vacuum and the state $|2\rangle$. For $\zeta = 0$, one has $G^{(2)} = F^2/\chi$ for $\Delta = \chi$. This formula can be generalized to obtain $G^{(n)}$ for an arbitrary $|0\rangle \rightarrow |n\rangle$ transitions [50]. The dissipation maintains its form, instead.

1. Strong modulation case

We first choose $\Omega \gg |\chi|$ (strongly modulated case). In Figs. 4 (a-c) we report the scattering coefficient $|S_{21}|$ as a function of the detuning Δ and the strength ζ of the modulation. As the drive amplitude F is increased, several additional dips appear, signaling the transitions between the photon number states $|0\rangle$ and $|n\rangle$ of the resonator. These dips occur at a frequency lower than each main LZSM dip associated with the transition $|0\rangle \rightarrow |1\rangle$. Each new additional dip is detuned by the same frequency as the unmodulated multiphoton resonances shown in Figs. 2 (c-e). Within a first approximation, this effect is due to the interplay between the modulation in Eq. (3)

and the nonlinearity of the system, as shown in Fig. 4 (d) reporting the result of a numerical simulation.

To explain this behavior, we can assume that, around each of the LZSM dips, we again have a drive of the same form as Eq. (3). When we then match the condition for a multiphoton resonance, it is this effective drive that leads to the excitation of the state $|2\rangle$. One then obtains

$$\hat{H}_{\bar{m}}^{(2)}/\hbar = 2[-\Delta_{\bar{m}}^{(2)} + \chi]|2\rangle\langle 2| + G_{\bar{m}}^{(2)}(|0\rangle\langle 2| + \text{h.c.}), \quad (7)$$

where [50]

$$\Delta_{\bar{m}}^{(2)} = \Delta - \bar{m}\Omega, \quad G_{\bar{m}}^{(2)} \simeq \frac{F_{\bar{m}}^2}{\chi} = \frac{F^2}{\chi} \left[J_{\bar{m}} \left(\frac{\zeta}{\Omega} \right) \right]^2. \quad (8)$$

This formula can be generalized to arbitrary n -photon resonances with $\Delta_{\bar{m}}^{(n)} = \Delta - \bar{m}\Omega$ and $G_{\bar{m}}^{(n)} \propto (J_{\bar{m}}(\zeta/\Omega))^n$. We conclude that when the rescaled detuning matches the condition for the n th multiphoton resonance, and if the rescaled drive $F_{\bar{m}}$ is strong enough, an additional dip appears. Therefore, we can treat each of the multiphoton resonances for each LZSM dip as a yet separate phenomenon.

As sketched in Figs. 4 (e-g), at the multiphoton resonance, i.e., at $\Delta = m\Omega + (n-1)\chi$, the states $|0\rangle$ and $|2\rangle$ can satisfy the conditions for the development of constructive interference. In other words, around each of the main LZSM dips, and for large enough drive amplitude, several multiphoton resonances emerge with the same characteristics as those shown in Figs. 2 (c-e).

2. Weak modulation case

When $\Omega \ll |\chi|$ (weakly modulated case), instead, one can capture the system's behavior around the second multiphoton resonance via the Hamiltonian in Eq. (6), with $G^{(2)} = F^2/\chi$ representing the effective drive between the vacuum and the state $|2\rangle$ if $\zeta = 0$. Removing the modulation using the same approximation as in Eq. (3) leads to an equation identical to Eq. (7), where now

$$\Delta_{\bar{m}}^{(2)} = (\Delta - \bar{m}\Omega/2), \quad G_{\bar{m}}^{(2)} = \frac{F^2}{\chi} J_{\bar{m}} \left(\frac{2\zeta}{\Omega} \right). \quad (9)$$

This formula can be generalized to arbitrary n -photon resonances, with $\Delta_{\bar{m}}^{(n)} = \Delta - \bar{m}\Omega/n$ and $G_{\bar{m}}^{(n)} \propto J_{\bar{m}}(n\zeta/\Omega)$. Thus, for detunings close to the n th multiphoton transition, a new LZSM interference pattern should emerge, characterized by an effective modulation frequency Ω/n . It is this scaling that differentiates the weakly and strongly modulated cases, c.f. Figs. 5 (a,e) and Fig. 4 (d). While previously the system displayed repeated copies of the multiphoton resonance around the LZSM dips of the $|0\rangle \rightarrow |1\rangle$ resonance, here each multiphoton resonance produces its own LZSM interference pattern distinguished from $|0\rangle \rightarrow |1\rangle$.

For the device under consideration, accessing the weakly modulated case would require $\kappa \ll \Omega/n$ to distinguish between the different LZSM dips. To better resolve this feature, we propose the following driving scheme. We fix the ratio ζ/Ω to have a constant effective drive, according to both effective theories in Eqs. (3) and (7). We then increase Ω and ζ , to cross from the weakly modulated $|\chi| > \Omega$ to the strongly modulated case $|\chi| < \Omega$. This is shown in Figs. 5 (b-d) where, for small Ω , we distinctly see the expected LZSM dips associated with the second multiphoton resonance $|0\rangle \rightarrow |2\rangle$ and with a slope $\Omega/2$

3. Non-perturbative regime

The weak- and strong-modulation regimes are completely different from each other [c.f. the effective models in Eqs. (8) and (9)]. We thus expect that there is a *non-perturbative passage* from weak- to strong-modulation through some effective interaction, and the transition between these two regimes cannot be explained using any of the two effective theories alone.

Particularly interesting are the values of $\Omega \simeq n|\chi|$, where the system passes from the weak- to the strong-modulated case for a specific state $|n\rangle$. At these values, it is possible for a n -photon resonance to exactly match the LZSM dips of a different m -photon resonance. We observe the signatures of avoided level crossings between resonances in Figs. 5(b-c), indicating that the $|0\rangle \rightarrow |1\rangle$ and $|0\rangle \rightarrow |2\rangle$ resonances interact through the action of an effective emergent coupling. In this sense, these different resonances constitute a *controllable synthetic Floquet space*, where changing Ω and ζ allows selecting an effective interaction between these multiphoton resonances. This is also evident in Fig. 5 (d), where the ratio Ω/ζ is changed, leading both to different interference patterns and different splittings between the Floquet states.

To further highlight an example of these non-perturbative effects, in Figs. 5 (f-g) we fix $\Omega = |\chi|$. First, we numerically simulate the interplay of these effects in Fig. 5 (f). We predict a partial overlap between the second multiphoton transition $|0\rangle \rightarrow |2\rangle$ with the first LZSM dip associated with the $|0\rangle \rightarrow |1\rangle$ transition at $\Delta = -\Omega$. For increasing modulation strength ζ , the LZSM structure predicted by Eq. (7) is observed, although strongly deformed compared to the prediction of the effective model due to the presence of the LZSM lobe associated with the $|0\rangle \rightarrow |1\rangle$ resonance. These theoretical predictions are completely recovered in the data in Fig. 5 (g). Finally, in Fig. 5 (h) we fix $\Omega = 1.5|\chi|$, and we observe a line splitting of several resonances, indicating again the merging and interaction between $|0\rangle \rightarrow |2\rangle$ and $|0\rangle \rightarrow |1\rangle$ transitions. For larger drive amplitudes (not shown), the system shows an extremely rich structure that cannot be simply assigned to any of these original phenomena. Note also the asymmetric nature of the interference pattern, determined by the negative sign of the Kerr nonlinearity.

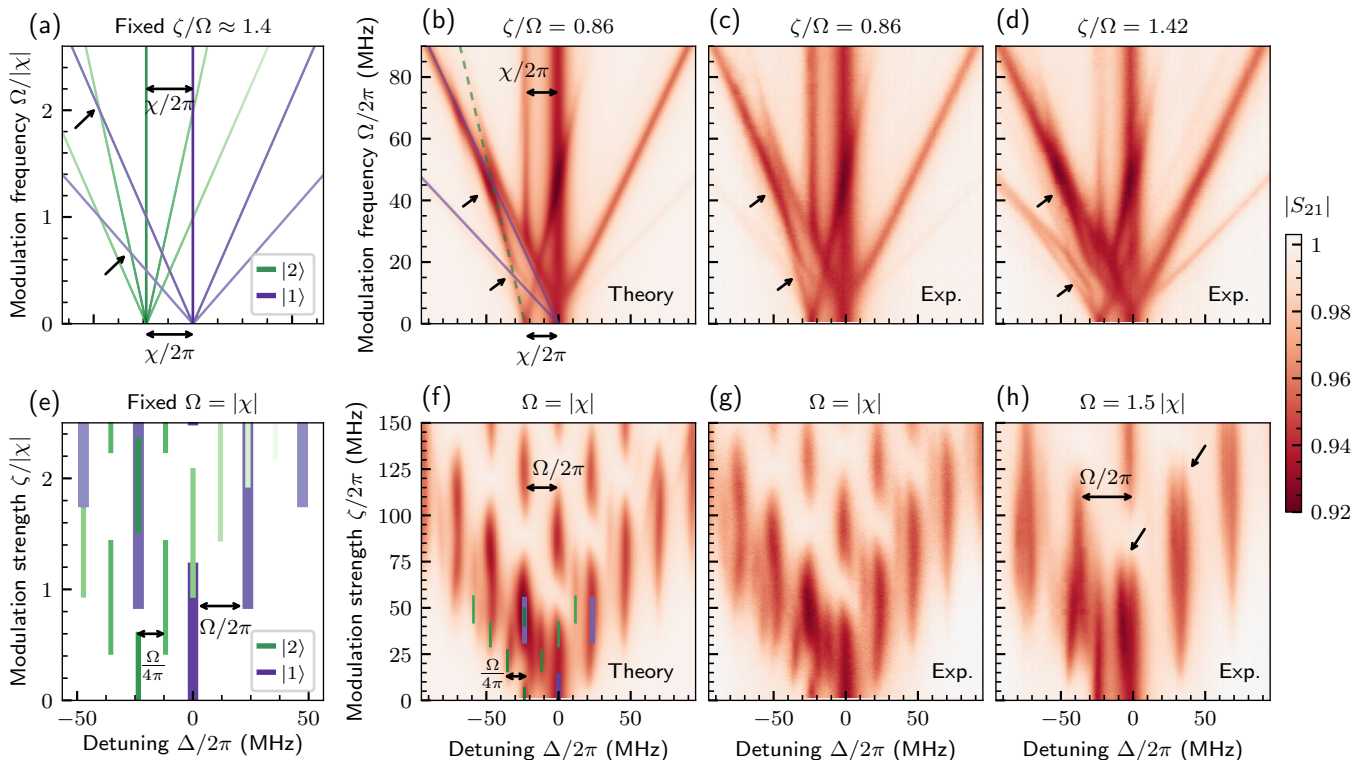


FIG. 5. Controllable Floquet states with the $N = 10$ device in the Kerr regime. Through the figure, we set the drive input power to $P_{\text{in}} = -128$ dBm. (a-d) Both modulation strength ζ and frequency Ω are swept together to maintain a constant ratio ζ/Ω . This choice ensures that the effective drives in Eqs. (3) and (7) are kept constant. This allows enhancing the visibility of the transition between the strongly- and weakly-modulated cases. (a) Sketch of the results of Eq. (7) for the transition $|0\rangle \rightarrow |1\rangle$ (purple, labeled |1>) and $|0\rangle \rightarrow |2\rangle$ (green, labeled |2>). For |1>, the pattern radiates from $\Delta = 0$ with frequency modulation Ω . For the multiphoton transition to |2>, the LZSM interference pattern is centered at $\Delta = \chi$ and scales with $\Omega/2$. (b) Simulation of $|S_{21}|$ as a function of Δ and Ω with the full quantum model in Eq. (2) (see Appendix A for details on the simulation method), having fixed $\zeta/\Omega = 0.86$. The corresponding measurement is shown in panel (c) and perfectly overlaps with the numerical simulation. The black arrows in (a-d) mark the position of two avoided crossings, where the “bare levels” in (a) interact and hybridize in (b-d). The crossings are further highlighted by the solid (associated with |1>) and dashed (|2>) lines in (b). The amplitude of the different avoided crossings can be controlled by modulating the Bessel functions $J_{\bar{m}}(n\zeta/\Omega)$ as shown in (d), where a larger ratio ζ/Ω is chosen. (e) As in panel (a), the sketch of the results of Eq. (7) for $\Omega = |\chi|$ and as a function of Δ and ζ . In this “bare picture”, the two independent LZSM interference patterns scale with Ω and $\Omega/2$ for |1) and |2), respectively. (f) Full quantum simulation and (g) corresponding measurement of $|S_{21}|$ for $\Omega = |\chi|$. The position of some LZSM resonances in the bare picture is superimposed in (f) as a guideline for the eye. (h) Repeating the measurement for $\Omega = 1.5|\chi|$, we observe line splittings, indicating a modulation of the coupling between different Floquet states.

B. Duffing regime

Finally, we investigate the Duffing regime $\kappa > |\chi|$ for a drive amplitude sufficiently large to deviate from the linear regime [49]. For the intermediate drive amplitudes shown in Figs. 6 (a) and (b), the various dips are well separated despite showing an asymmetric bending of $|S_{21}|$. When compared with Figs. 2 (g) and (h), we observe a similar deformation of the transmission dips. Therefore, we assign this feature to the emergence of *bistability triggered by the competition between detuning and Kerr non-linearity*. For these parameters, we find that the formula in Eq. (3) captures the deformation of the dips, as discussed more in detail in Appendix A 3. Thus, the system behaves as a collection of independent Duffing oscillators

and the overall effect of the modulation is to rescale the drive amplitude F .

When the driving power is further increased in Fig. 6 (c), several of the neighboring LZSM dips eventually overlap. This case cannot be simply captured as separated LZSM interferences, and it is qualitatively different from all the previously studied cases. The simplified picture of Eq. (3) thus breaks down, and the system becomes multimodal and behaves as a set of interacting nonlinear cavities. Nonetheless, the full simulation of the quantum Floquet model matches the data in all regimes, as shown in Figs. 6 (d-f).

This picture is further confirmed when investigating LZSM interference for three values of modulation strength ζ as a function of the driving power P_{in} , as

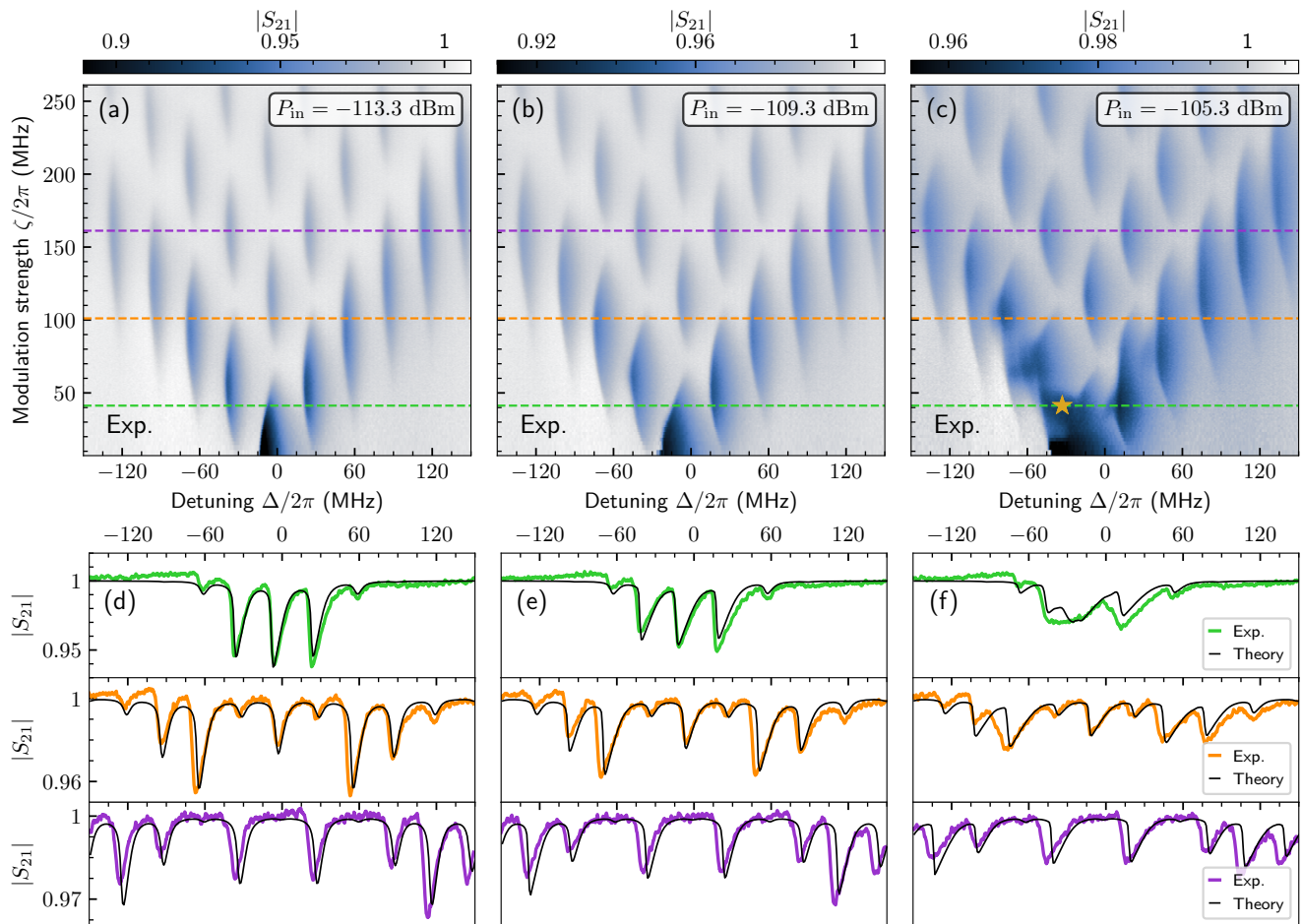


FIG. 6. LZSM interferometry with the $N = 32$ device in the Duffing regime. (a-c) Measured magnitude of S_{21} versus Δ and ζ for increasing drive power P_{in} . The dashed color lines refer to the values of ζ chosen for panels (d-f). The star in (c) indicates the value where the analysis of chaos is performed in Fig. 7(d). (d-f) Measured S_{21} as a function of detuning and for three specific values of $\zeta/2\pi$: 41.3 MHz (green curve), 101.1 MHz (orange curve), and 161.2 MHz (purple curve). The black superimposed curves are the results of the numerical simulation of the full quantum model for the parameters in Table I (detailed in Appendix A 1 a). The modulation frequency is set to $\Omega/2\pi = 30$ MHz. The systematic discrepancy in the position of the dips between theory and experiments is due to the nonlinear dependence of the modulation of the flux amplitude discussed in Appendix B.

shown in Figs. 7 (a-c). At low driving power, we find a linear regime where m dips appear separated by the frequency $\Omega/2\pi = 30$ MHz and with visibility given by Bessel functions $J_m(\zeta/\Omega)$. This regime is remarkably similar to that of several nonlinear modes separated by the same frequency Ω . As the driving power increases, each of these dips initially follows the typical Duffing behavior of a single resonator, as already mentioned. For high enough input power, however, these individual dips disappear and merge, leading to a very broad response of the system. At this point, one completely loses the notion of individual synthetic modes and their bistability. As detailed in Ref. [40], when two or more nonlinear driven cavities merge, dissipative quantum chaos arises.

We theoretically verify that at the point where the multiple resonances of the LZSM Duffing regime merge, a

chaotic structure of the system can be observed. The theoretical analysis is detailed in the Appendix A 2, and involves a Floquet Liouvillian analysis. In Fig. 7 (d) we remark that, as soon as the merging of the Floquet modes occurs, the Floquet Liouvillian level statistics follows the Ginibre distribution [see Eq. (A15)] associated with dissipative quantum chaos [51]. Notice also that, to get a qualitative and quantitative agreement between theory and experimental observations, the theoretical framework presented in Ref. [40] is essential. As detailed in Appendix A 2, we can observe how the emergence of a chaotic regime coincides exactly with the merging of the resonances.

The onset of the chaotic phase can also be controlled by tuning the spacing between LZSM resonances through the modulation frequency Ω , as shown in Appendix C.

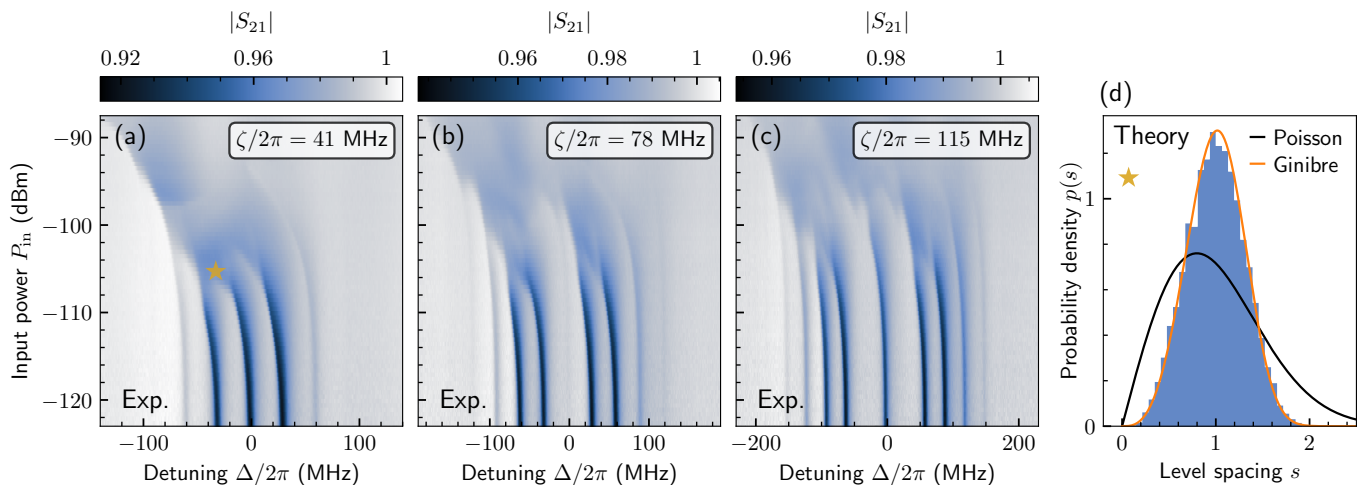


FIG. 7. Multimodal-like behavior in the Duffing regime. (a-c) Measurement of $|S_{21}|$ for increasing drive power, fixed frequency modulation $\Omega/2\pi = 30$ MHz and increasing ratios $\zeta/\Omega \approx 1.4$ (a), $\zeta/\Omega \approx 2.6$ (b) and $\zeta/\Omega \approx 3.8$ (c). For low input powers the system behaves as a collection of noninteracting nonlinear modes, each one well separated from the others. For larger values of P_{in} , the system enters a phase characterized by a single broad response where the notion of isolated mode is lost. Such a response can be observed in multimode nonlinear systems and has been associated with a transition from integrability to dissipative quantum chaos [40]. To show that this is indeed a dissipative quantum chaotic phase we plot in (d) the histogram of the probability density $p(s)$ of the level spacings s obtained by diagonalizing the Floquet Liouvillian in the broad-response region indicated by the star in panel (a). Details are provided in the Appendix A 2. Parameters are set to $\zeta/2\pi = 41.3$ MHz, $\Omega/2\pi = 30$ MHz, $\Delta = -1.1\Omega$ and $F/2\pi = 49.5$ MHz ($P_{in} \approx -105$ dBm). The cutoff in the Hilbert space is set to 90. The solid black (orange) curve represents the ideal Poisson (Ginibre) distribution given by Eq. (A14) [Eq. (A15)] associated with integrability (chaos).

For instance, the separated bistable regions of Fig. 6 (b) would start overlapping by decreasing Ω , potentially resulting in a chaotic state.

V. CONCLUSIONS

This article investigates the physics of Landau-Zener-Stückelberg-Majorana (LZSM) interference beyond the conventional two-level approximation. By employing two nonlinear superconducting resonators—one in the Kerr (nonlinearity larger than dissipation rate) and the other in the Duffing (nonlinearity smaller than dissipation rate) regime—we have established a general paradigm for studying LZSM interference in bosonic systems. We have developed a unified model that accurately describes the observed phenomena across all parameter regimes before the onset of many-body-like effects.

At low driving powers, we have shown that interference patterns remain independent of the system nonlinearity, preventing the distinction between linear and nonlinear resonators. However, at higher driving powers, we have uncovered novel effects arising from the interplay between modulation and nonlinearity, with the dissipation rate playing a crucial role in shaping the emergent features.

In the Kerr regime, our experiments have highlighted the influence of Kerr multiphoton resonances on the LZSM interference pattern, leading to the formation of avoided level crossings between Floquet states. Con-

versely, in the Duffing regime, we have theoretically demonstrated and witnessed the effects of the emergence of optical bistability. We have then theoretically shown that the onset of dissipative quantum chaos in the Floquet regime coincides with a qualitative change in the resonator’s properties.

Overall, our work significantly advances the current understanding of LZSM and Floquet physics, shedding light on the intricate interplay between interference and nonlinear effects. Furthermore, our findings pave the way for controlling and engineering Floquet states and synthetic dimension engineering. The highly tunable nature of the system opens exciting avenues for future research in quantum dynamics and quantum control.

As future perspectives, the merging of multiple interference peaks both in the Kerr and Duffing regimes offers several potential applications. In the Kerr regime, we show the presence of an “effective interaction” between Floquet states, that can be either enabled or suppressed by tuning the modulation parameters. These could be used to, e.g., engineer transition and interaction between states with different decay rates, and provide opportunities to simulate non-Markovian baths [52]. Conversely, in the Duffing regime, this Floquet approach to dissipative chaos has reduced susceptibility to disorder and fabrication mismatches when compared to alternative implementations in extended systems [53–55]. This opens possibilities to use this LZSM interference to simulate emergent chaotic features in engineered dissipative

and time-dependent configurations, such as ultrastrongly coupled light-matter systems [56, 57], devices in the noisy intermediate-scale quantum (NISQ) era [41, 42], and two-photon driven systems [36, 58]. Finally, LZSM protocols have been used as quantum simulators of Kibble-Zurek mechanisms [59, 60]. The extension of a similar protocol to multilevel phenomena is still lacking.

ACKNOWLEDGMENTS

We thank Alberto Mercurio and Sergey Shevchenko for the useful discussion and the insights on the numerical coding. M.S. acknowledges support from the EPFL Center for Quantum Science and Engineering postdoctoral fellowship. F.N. is supported in part by: Nippon Telegraph and Telephone Corporation (NTT) Research, the Japan Science and Technology Agency (JST) [via the Quantum Leap Flagship Program (Q-LEAP), and the Moonshot R&D Grant Number JPMJMS2061], the Asian Office of Aerospace Research and Development (AOARD) (via Grant No. FA2386-20-1-4069), and the Office of Naval Research (ONR) Global (via Grant No. N62909-23-1-2074). V.S. acknowledges support by the Swiss National Science Foundation through Projects No. 200020_185015 and 200020_215172. P.S. and V.S. acknowledge support from the EPFL Science Seed Fund 2021 and of Swiss State Secretariat for Education, Research and Innovation (SERI) under contract number UeM019-16. P.S. acknowledges support from the Swiss National Science Foundation through Projects No. 206021_205335 and Projects No. 200021_200418, and from the SERI through grant under contract number MB22.00081.

Appendix A: Theoretical and numerical methods

1. Construction and solution of the Floquet-Liouvillian problem

The periodically modulated systems in Eq. (2) can be described using a stroboscopic Lindblad master equation of period T . The equation of motion of such a system is

$$\hbar\partial_t\hat{\rho}(t) = \mathcal{L}(t)\hat{\rho}(t), \quad \mathcal{L}(t+T) = \mathcal{L}(t). \quad (\text{A1})$$

While the temporal dependence of $\mathcal{L}(t)$ prevents the emergence of a true steady state, one can still reach a *stroboscopic* stationary regime.

a. The average Floquet steady-state

We are interested in the average properties of the system along one modulation period $T = 2\pi/\Omega$ after a time long enough for the system to have reached a stroboscopic stationary regime.

To solve this problem, we assume that, for a long enough time,

$$\hat{\rho}(t) = \sum_{m=-\infty}^{+\infty} \hat{\rho}_m e^{im\Omega t}. \quad (\text{A2})$$

One can easily verify that

$$\frac{1}{T} \int_t^{t+T} \hat{\rho}(\tau) d\tau = \hat{\rho}_0. \quad (\text{A3})$$

At this point, one has to determine $\hat{\rho}_0$. A convenient way to find it is to solve it through Fourier analysis (see, e.g., [61, 62]).

The equation of motion can be recast as

$$\begin{aligned} \hbar \frac{d}{dt} \hat{\rho}(t) &= \sum_{m=-\infty}^{+\infty} im\Omega \hat{\rho}_m e^{im\Omega t} \\ &= [\mathcal{L}_0 + \mathcal{L}_1 e^{i\Omega t} + \mathcal{L}_{-1} e^{-i\Omega t}] \hat{\rho}(t) \\ &= \sum_{m=-\infty}^{+\infty} [\mathcal{L}_0 + \mathcal{L}_1 e^{i\Omega t} + \mathcal{L}_{-1} e^{-i\Omega t}] \hat{\rho}_m e^{im\Omega t}, \end{aligned} \quad (\text{A4})$$

where \mathcal{L}_0 is the time-independent part of the Liouvillian in Eq. (2) (i.e., $\zeta = 0$), while \mathcal{L}_1 and \mathcal{L}_{-1} represent the decomposition of the modulation. Collecting each term evolving with Ω we have

$$\sum_{m=-\infty}^{+\infty} [(\mathcal{L}_0 - im\Omega) \hat{\rho}_m + \mathcal{L}_1 \hat{\rho}_{m-1} + \mathcal{L}_{-1} \hat{\rho}_{m+1}] e^{im\Omega t} = 0. \quad (\text{A5})$$

If we now assume that each term of the sum is stationary, we obtain the recursion relation

$$(\mathcal{L}_0 - im\Omega) \hat{\rho}_m + \mathcal{L}_1 \hat{\rho}_{m-1} + \mathcal{L}_{-1} \hat{\rho}_{m+1} = 0. \quad (\text{A6})$$

By truncating this recursion (i.e., assuming $\hat{\rho}_m = 0$ if $m > M$ or $m < -M$), the problem can be then self-consistently solved.

b. Analysis of the Floquet Liouvillian spectrum

A different approach to solving the Floquet problem consists of constructing the so-called *Floquet evolution superoperator* (a Floquet map for Lindbladian systems). Indeed, using the time ordering \mathcal{T} , we can formally solve Eq. (A1) as

$$\hat{\rho}(t) = \mathcal{T} \left[\exp \left(\int_0^t \mathcal{L}(t') dt' / \hbar \right) \right] \hat{\rho}(0) = \mathcal{F}(t, 0) \hat{\rho}(0). \quad (\text{A7})$$

$\mathcal{F}(t, t_0)$ is the evolution superoperator for the time-dependent Lindblad master equation. We can then formally introduce the Floquet Liouvillian \mathcal{L}_F as

$$\mathcal{F}(T, 0) = \exp(\mathcal{L}_F T / \hbar). \quad (\text{A8})$$

The stroboscopic steady state is the state such that

$$\mathcal{L}_F \hat{\rho}_{ss}^F = 0, \quad \text{or} \quad \mathcal{F} \hat{\rho}_{ss}^F = \hat{\rho}_{ss}^F. \quad (\text{A9})$$

To construct $\mathcal{F}(T, 0)$ [63], let us consider

$$\mathcal{F}(T, 0) \hat{\rho}_{i,j}, \quad \hat{\rho}_{i,j} = |i\rangle\langle j|. \quad (\text{A10})$$

Since $\hat{\rho}_{i,j}$ are an orthonormal basis of the operators space (i.e., any operator can be written as a linear combination of $\hat{\rho}_{i,j}$), we conclude that the matrix form of $\mathcal{F}(T, 0)$ can be obtained as

$$\mathcal{F}_{[m=i:(N+1)+j,:]} = \text{vec}[\hat{\rho}_{i,j}(T)], \quad (\text{A11})$$

where $\mathcal{F}_{[m,:]}$ indicates the m th row of the evolution operator in its matrix form, and $\text{vec}[\hat{\rho}_{i,j}(T)]$ is the vectorized form of the initial density matrix $\hat{\rho}_{i,j}$ evolved for a time T .

2. Analysis of dissipative quantum chaos

To determine the chaotic or integrable nature of the system, we extend the methods in Ref. [40] to Floquet systems. The Floquet Liouvillian superoperator \mathcal{L}_F can be diagonalized obtaining its right (left) eigenvectors $\hat{\eta}_j$ ($\hat{\sigma}_j$) and the Liouvillian spectrum $\{\lambda_j\}$

$$\mathcal{L}_F \hat{\eta}_j = \lambda_j \hat{\eta}_j, \quad \mathcal{L}_F^\dagger \hat{\sigma}_j = \lambda_j^* \hat{\sigma}_j, \quad (\text{A12})$$

which satisfy the bi-orthonormality condition $\text{Tr}\{\hat{\sigma}_j^\dagger \hat{\eta}_l\} = \delta_{jl}$.

Integrability and dissipative quantum chaos in the open quantum system can be characterized via the statistical distribution of the spacings of the complex Liouvillian eigenvalues $\{\lambda_j\}$ [51]. In particular, one studies the distribution of nearest-neighbor eigenvalue spacings

$$p(s) = \sum_j \delta(s_j - s), \quad (\text{A13})$$

where $s_j = |\lambda_j - \lambda_j^{\text{NN}}|$, with λ_j^{NN} the eigenvalue closest to λ_j in the complex plane.

a. Level statistics

In integrable dissipative systems, s follows a 2D Poisson distribution

$$p_{2D}(s) = \frac{\pi}{2} s e^{-\frac{\pi}{4} s^2}, \quad (\text{A14})$$

while for chaotic dissipative systems the level spacing distribution follows the Ginibre distribution of Gaussian non-Hermitian random matrices ensembles

$$p_{\text{GinUE}}(s) = \left(\prod_{k=1}^{+\infty} \frac{\Gamma(1+k, s^2)}{k!} \right) \sum_{j=1}^{+\infty} \frac{2s^{2j+1} e^{-s^2}}{\Gamma(1+j, s^2)}. \quad (\text{A15})$$

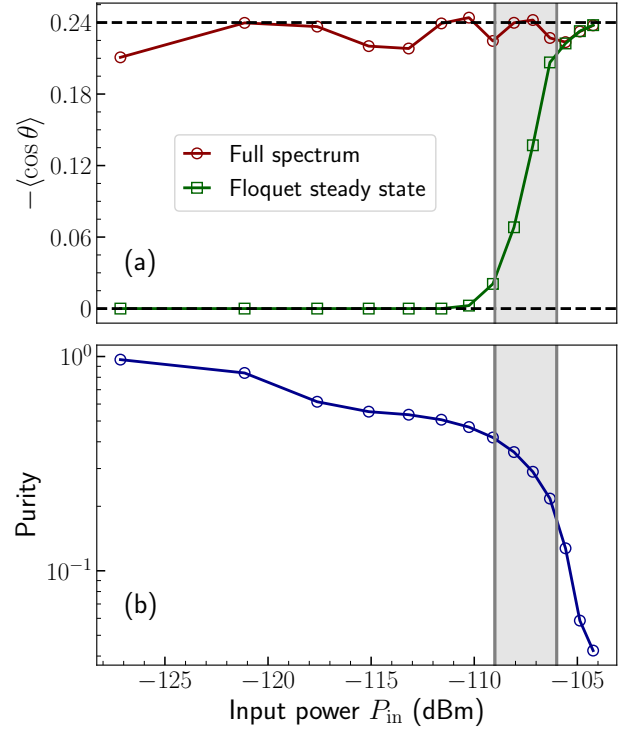


FIG. 8. Analysis of dissipative quantum chaos using the SSQT criterion detailed in Ref. [40] and generalized to Floquet states here. (a) Theoretical indicator of chaos $\langle \cos \theta \rangle$ introduced in Ref. [66] computed on the full Floquet-Liouvillian spectrum (red line) and on the eigenvalues selected by the SSQT criterion as discussed in Appendix A 2 (green line). While the spectral analysis on the full Liouvillian indicates the presence of chaos independently of the drive amplitude for the parameters considered in the plot, the SSQT criterion identifies the broadening of the Duffing peaks in Fig. 7 (a-c) (grey rectangle) with a dissipative quantum chaotic phase for the Floquet steady state $\hat{\rho}_{ss}^F$. When the number of selected eigenvalues is smaller than 100 a statistically significant analysis can not be carried out, and we set $\langle \cos \theta \rangle = 0$. (b) Purity $\text{Tr}[(\hat{\rho}_{ss}^F)^2]$ of the Floquet steady state $\hat{\rho}_{ss}^F$. The onset of steady-state quantum chaos in panel (a) coincides with the drop of the purity of the steady state below 0.1. We use the parameters of Fig. 7 (a), the cutoff in the Hilbert space is fixed to 90, and c_{min} is selected according to [67].

An unfolding procedure, in which the uncorrelated part is removed from $p(s)$ in Eq. (A13), is required to evaluate the level statistics from the spectrum and for the proper characterization of chaos [64]. We adopt that described in Ref. [65].

An alternative, efficient way to perform this analysis is the complex spacing ratio [66]

$$z_j = \frac{\lambda_j^{\text{NN}} - \lambda_j}{\lambda_j^{\text{NNN}} - \lambda_j} = r_j e^{i\theta_j}, \quad (\text{A16})$$

with λ_j^{NN} the eigenvalue closest to λ_j in the complex plane, and λ_j^{NNN} the second-nearest neighbor to λ_j . The average values $\langle r \rangle$ of r and $\langle \cos \theta \rangle$ of $\cos \theta_j$, can be used

as indicators of dissipative quantum chaos. For a 2D Poisson distribution, associated with an integrable system, $\langle r \rangle = 0.66$, and $-\langle \cos \theta \rangle = 0$. For the Ginibre distribution, i.e., chaos, $\langle r \rangle = 0.74$, and $-\langle \cos \theta \rangle = 0.24$.

The above spectral signatures alone, however, do not correctly capture the emergence of dissipative quantum chaos in the system considered in this work. For instance, in Fig. 8 (a) we plot the indicator $\langle \cos \theta \rangle$ as a function of the input power P_{in} . For these input powers, the prediction of the spectral analysis of the Floquet Liouvillian is that the system is *always* in a chaotic phase, despite it being almost a pure state for weak P_{in} [c.f. Fig. 8 (b)]. We conclude that this straightforward analysis of chaos cannot capture the relevant features of the model under consideration.

b. Spectral statistics of quantum trajectories for Floquet systems

Here, we generalize the theoretical framework of the spectral statistics of quantum trajectories (SSQT) introduced in Ref. [40]. First, one remarks that the Lindblad master equation admits also a stochastic unraveling in terms of quantum trajectories $|\psi(t)\rangle$, combining the Hamiltonian dynamics with a continuous monitoring of the environment [68, 69]. The wave function $|\psi(t)\rangle$ can be interpreted as a single stochastic realization of the dissipative dynamics whose average reproduces the predictions of the Lindblad master equation Eq. (2). As discussed in Ref. [40], since the system discussed in this article does not have any weak or strong Liouvillian symmetry, all the possible unravelings are expected to give the same information about steady-state integrability and chaos. We can therefore assume a diagonal unraveling which we can write down considering the spectral decomposition of the Floquet steady state

$$\hat{\rho}_{\text{ss}}^{\text{F}} = \sum_k p_k |\psi_k\rangle \langle \psi_k|. \quad (\text{A17})$$

Using the spectral decomposition introduced in Eq. (A12), one can then define

$$\hat{\rho}_k = |\psi_k\rangle \langle \psi_k| = \sum_j c_{k,j}(t) \hat{\eta}_j. \quad (\text{A18})$$

This procedure allows associating to each eigenvalue λ_j the relative spectral weight $c_{k,j}$. We select the Liouvillian eigenvalues λ_j , for which $|c_{k,j}(t)| > c_{\text{min}}$ [67]. On each $\hat{\rho}_k$ we perform the spectral analysis by computing, e.g., the complex spacing ratio for the selected eigenvalues $\langle \cos \theta \rangle_k$. We finally obtain $\langle \cos \theta \rangle = \sum_k p_k \langle \cos \theta \rangle_k$.

In Fig. 8 (a), the green curve represents the results of the SSQT criterion. Compared to the spectral statistics applied to the full Floquet Liouvillian spectrum, we see a profoundly different behavior of the system as a function of the drive amplitude. Notably, the onset of dissipative chaos in the Floquet steady state coincides

with the merging and broadening of the dips of the scattering coefficient $|S_{21}|$ in Fig. 7 (a-c), as indicated by the grey rectangle. Comparing the results of Fig. 8 (a) with the purity of $\hat{\rho}_{\text{ss}}^{\text{F}}$ in Fig. 8 (b), this time we observe that it drops below 0.1 only when we enter the steady-state chaotic region. This result ultimately demonstrates the necessity of the SSQT criterion to correctly interpret the onset of chaos in open quantum systems.

3. Derivation of an effective model for the study of the nonlinear modulated resonators

To simplify the equation of motion, we want to eliminate the frequency modulation. To do this, we use the interaction picture $\hat{\rho}(t) = \hat{U}^\dagger(t) \hat{\rho} \hat{U}(t)$, where

$$\begin{aligned} \hat{U}(t) &= \mathcal{T} \exp \left[\int_0^t -i dt' \zeta \cos(\Omega t') \hat{a}^\dagger \hat{a} \right] \\ &= \exp \left[-i \frac{\zeta}{\Omega} \sin(\Omega t) \hat{a}^\dagger \hat{a} \right]. \end{aligned} \quad (\text{A19})$$

We obtain

$$\hbar \partial_t \hat{\rho}(t) = -i [\hat{H}, \hat{\rho}(t)] + \kappa \mathcal{D} \hat{a} \hat{\rho}(t) + \kappa_\phi \mathcal{D} \hat{a}^\dagger \hat{a} \hat{\rho}(t), \quad (\text{A20})$$

where

$$\begin{aligned} \hat{H}/\hbar &= \Delta \hat{a}^\dagger \hat{a} + \chi \hat{a}^\dagger \hat{a}^\dagger \hat{a} \hat{a} \\ &+ F \left\{ \hat{a} \exp \left[-i \frac{\zeta}{\Omega} \sin(\Omega t) \right] + \text{h.c.} \right\}. \end{aligned} \quad (\text{A21})$$

Equations (A20) and (A21) can be straightforwardly derived thanks to

$$\hat{U}^\dagger(t) \hat{a} \hat{U}(t) = \hat{a} \exp \left[-i \frac{\zeta}{\Omega} \sin(\Omega t) \right]. \quad (\text{A22})$$

We finally use the Jacobi-Anger expansion, reading

$$e^{iz \sin \theta} \equiv \sum_{m=-\infty}^{\infty} J_m(z) e^{im\theta}, \quad (\text{A23})$$

where $J_m(z)$ is the m th Bessel function of the first kind, to obtain (up to a phase)

$$\begin{aligned} \hat{H}/\hbar &= \Delta \hat{a}^\dagger \hat{a} + \chi \hat{a}^\dagger \hat{a}^\dagger \hat{a} \hat{a} \\ &+ \sum_{m=-\infty}^{\infty} F J_m \left(\frac{\zeta}{\Omega} \right) [\hat{a} e^{-im\Omega t} + \hat{a}^\dagger e^{im\Omega t}]. \end{aligned} \quad (\text{A24})$$

Notice that both dissipation and Kerr nonlinearity remain unchanged by this set of transformations.

Up to this point, no approximations have been made. For the small-drive amplitudes considered in Sec. III, however, we can assume that only one of the driving frequencies is relevant, and discard the fast-rotating terms. Namely, we select only those frequencies around which $\Delta_{\bar{m}} = \Delta - \bar{m}\Omega \simeq 0$, finally obtaining Eq. (3).

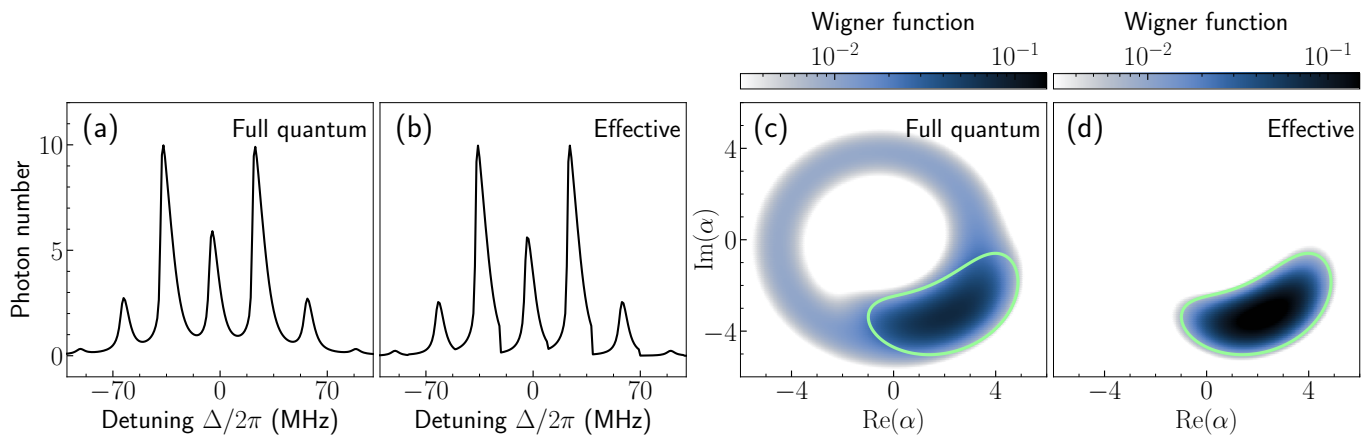


FIG. 9. Comparison between the full Floquet analysis and the effective model derived in Appendix A 3. We show the photon number n computed with the Floquet steady state [panel (a)] and with the effective Hamiltonian Eq. (3) [panel (b)]. The full quantum solution and the effective model exhibit a good agreement. We plot in panels (c) and (d) the Wigner function $W(\alpha) = 2/\pi \cdot \text{Tr} [\hat{D}_\alpha e^{i\pi \hat{a}^\dagger \hat{a}} \hat{D}_\alpha^\dagger \hat{\rho}]$, with $\hat{D}_\alpha = \exp(\alpha \hat{a}^\dagger - \alpha^* \hat{a})$, of the Floquet steady state and the effective model respectively. The green lines in panels (c) and (d) encircle the region where $W(\alpha) > 7 \times 10^{-3}$ according to the effective model. We conclude that the effective model is reliable when computing $\langle \hat{a}^\dagger \hat{a} \rangle$, i.e., the distance from the center of the distribution $W(\alpha)$. On the contrary, $\langle \hat{a} \rangle$ can not be captured by the simple treatment presented in Appendix A 3, as evident from the different angular distribution of $W(\alpha)$ obtained from the full and effective model. All physical parameters as in Fig. 6 (d). We set $\zeta/\Omega \approx 1.67$ and $\Delta/\Omega = -1.1$.

In Fig. 9 we benchmark the validity of the effective Hamiltonian given by Eq. (3) for the $N = 32$ device in the Duffing regime at intermediate input power. All the physical parameters have been chosen as in Fig. 6 (d). We compare the photon number n computed with the Floquet steady state [Fig. 9 (a)] and with the effective model [Fig. 9 (b)] showing that the two approaches exhibit a good agreement. While the approximation is remarkably predictive in determining the photon number, this is not the case for the coherence $\langle \hat{a} \rangle$. In Figs. 9 (c-d) we compute the Wigner functions obtained from the full quantum simulation of the Floquet steady state and that obtained according to the effective model. While the effective model nicely reproduces the radial distribution of the Wigner function (and thus the photon number), it completely misses the phase, which remains accessible only within the full Floquet-Lindblad treatment described in Appendix A 1 a. In both Figs. 9 (c) and (d) we report the contour of the effective Wigner function, showing that $W(\alpha)$ of the full quantum model contains the effective Wigner function, but the phase coherence is reduced with respect to the effective model. We argue that these dephasing-like effects are due to higher-order processes not accounted for in the effective model, emerging from the combination of Hamiltonian and dissipative terms, and treating them would require higher-order time-dependent perturbation theories such as the Floquet-Magnus expansion.

Appendix B: Experimental details

1. Fabrication

The devices are fabricated on a 525 μm thick high-resistivity intrinsic 4 inch silicon wafer. The substrate is cleaned using piranha solution, followed by the removal of native oxide via a 1% hydrofluoric acid treatment. Immediately after, a 150 nm thick layer of aluminum is deposited by e-beam evaporation at a rate of 0.2 nm s^{-1} . Alignment markers are defined through photolithography, e-beam evaporation of a 5 nm thick Ti layer and a 55 nm thick Pt layer, and subsequent lift-off. The waveguide and control lines are patterned via photolithography and wet etching for 2 min 30 s in TechniEtch Alu80 etchant. E-beam lithography is employed to define the Josephson junctions of the SQUID array. The wafer is coated with a bilayer resist stack consisting of 500 nm of MMA EL9 and 450 nm of PMMA 495K A8. The mask is then patterned using e-beam lithography (Raith EBPG5000+ at 100 keV) and developed in a 1:3 MIBK:IPA solution for 2 min. The Josephson junctions have a square shape with a width of approximately 350 nm. The Josephson junctions are formed by double-angle evaporation in an ultra-high vacuum Plassys MEB550SL3 system using the Manhattan technique [70]. This involves the deposition of 50 nm of aluminum at 0.5 nm s^{-1} at $+45^\circ$ tilt angle, followed by an oxidation step of 10 min in 0.15 Torr of pure dioxygen, a second aluminum deposition of 120 nm at 0.5 nm s^{-1} and -45° tilt angle, and a capping oxidation layer formed during 10 min in 4 Torr of pure O_2 . Lift-off is performed

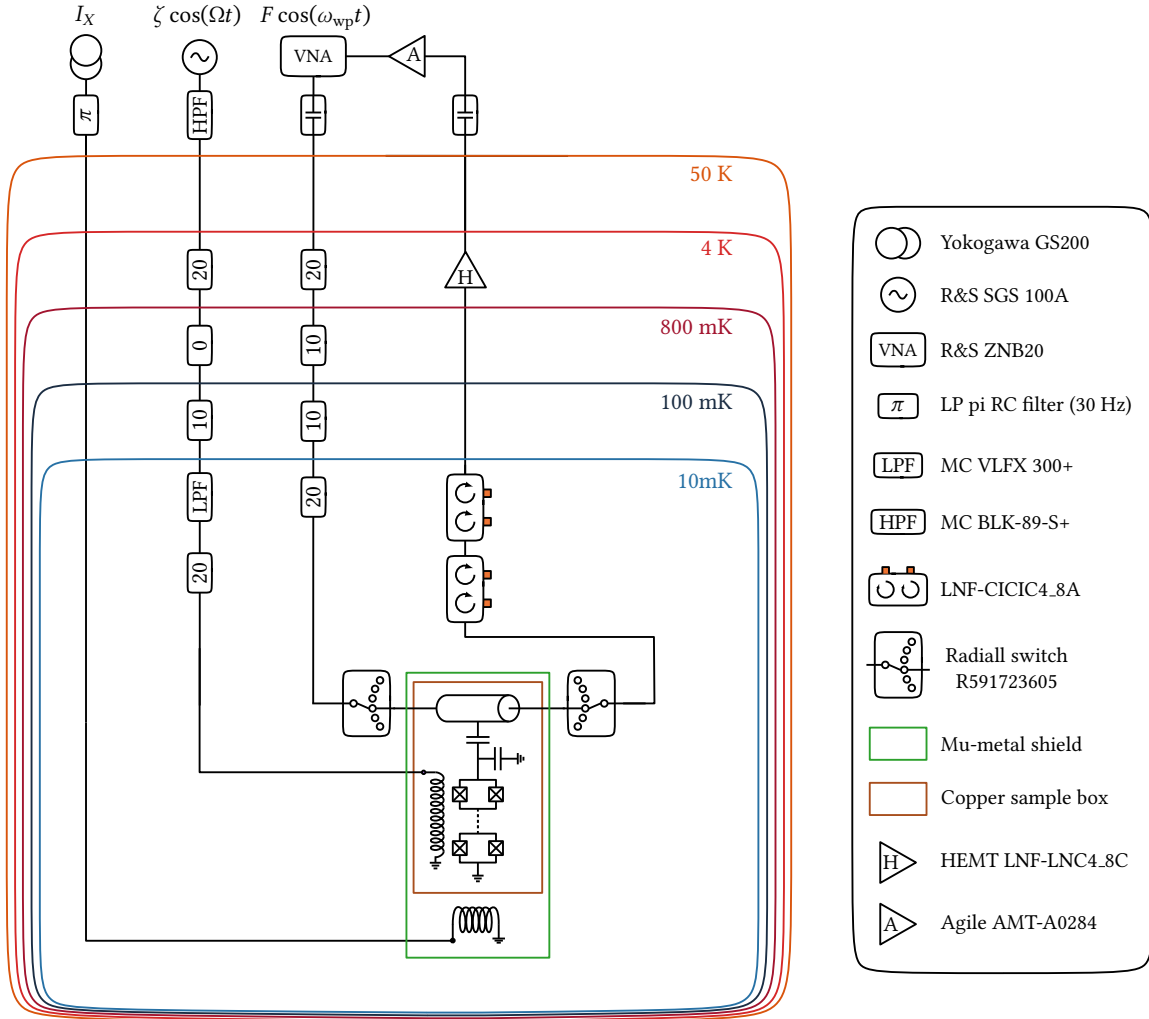


FIG. 10. Schematics of the full wiring of the cryostat and room-temperature electronics.

in 80 °C 1165 remover for 4 h to 8 h. A final patching step is carried out to close the loops of the isolated Josephson junctions formed with the Manhattan technique and to connect one side of the SQUID array to the ground plane. The same bilayer resist stack is used, and e-beam lithography is employed to expose the patch areas. The native oxide of the bottom aluminum layer is removed in the Plassys system by argon ion plasma milling, and a 200 nm thick aluminum layer is deposited directly after at a rate of 0.5 nm s^{-1} . Finally, the wafer is diced into $4 \times 7 \text{ mm}^2$ chips using a nickel-bonded diamond blade.

2. Measurement setup

A schematic of the measurement setup is shown in Fig. 10. The $4 \times 7 \text{ mm}^2$ die is wire bonded with aluminum wire on custom-printed circuit board. The die is then glued directly on a high-purity copper sample holder that is thermally anchored at the mixing chamber stage of a LD Bluefors cryostat with a typical base temper-

ature of 15 mK. The sample holder is protected against external magnetic fields using two mu-metal shields. The SQUID array is coupled to a 50 Ohm coplanar waveguide in a notch configuration. The input signal is generated by a vector network analyzer (VNA) R&S ZNB20 and transmitted via a heavily attenuated coaxial line to the device feedline. The output signal passes through two double-circulators before being amplified at 4K by a LNF-LNC4_8C HEMT amplifier and at room temperature by an Agile AMT-A0284 low-noise amplifier. The signal is collected and demodulated in the VNA. Six-ports Radiall R591723605 coaxial switches are placed on the mixing chamber plate on both sides of the feedline to allow switching between different devices. Both $N = 10$ and $N = 32$ devices presented in this work were connected between the same switches and thus shared the same input and output lines. The static flux of the SQUID array is controlled by applying a direct current to a NbTi external coil mounted underneath the sample holder. The direct current is applied via twisted NbTi pairs using a Yokogawa GS200 source. The frequency

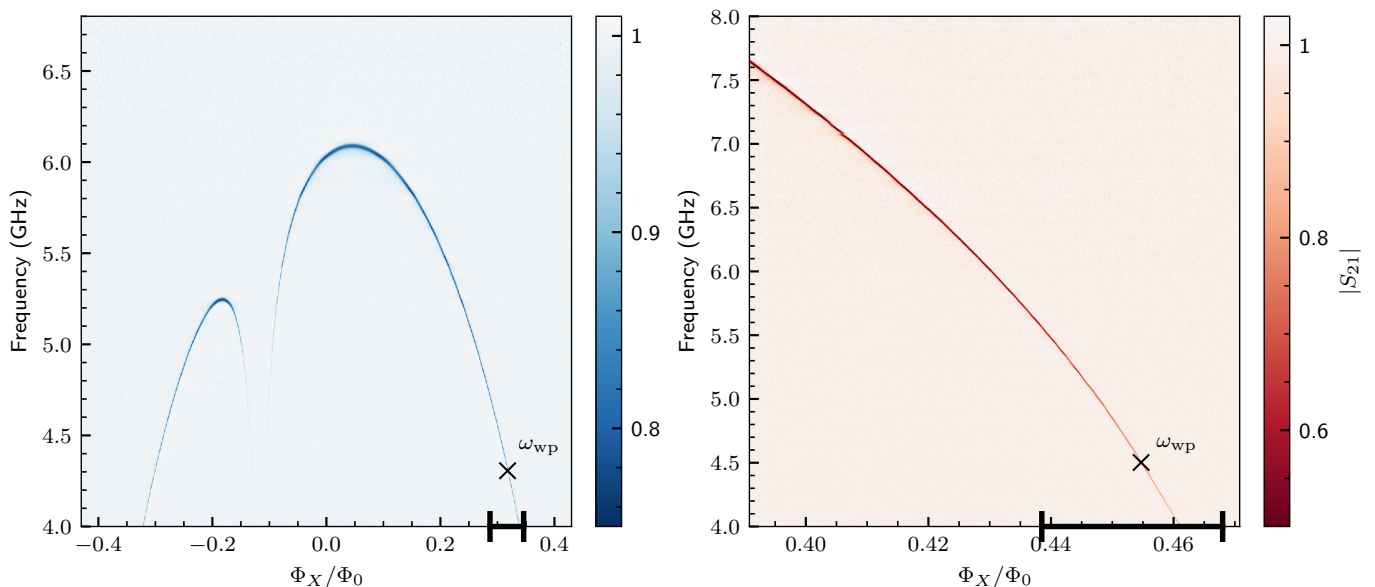


FIG. 11. Measurement of the magnitude of the transmission $|S_{21}|$ as a function of the flux Φ_X in the SQUID arrays for the $N = 32$ Duffing device (left, blue) and the $N = 10$ Kerr device (right, red). The flux working points used throughout the paper are indicated by cross markers. The black horizontal segments approximately denote the maximum flux modulation reported in this work with respectively ± 0.4 GHz and ± 1.1 GHz for the Duffing and Kerr devices.

modulation of the SQUID array is performed by applying a signal generated by a R&S SGS 100A signal generator to the local flux line of the device. The DC noise is attenuated using a high-pass filter with a cutoff frequency of 100 kHz at room temperature. The line is further attenuated and filtered at the mixing chamber stage with a Minicircuits VLFX-300+ low-pass filter (LPF). We found that without this LPF, the internal loss rate of the SQUID arrays was increased by up to a factor of ten. We also included an additional 20 dB of attenuation between the LPF and the flux line to eliminate spurious standing wave modes between the LPF and the on-chip ground termination of the flux line. Devices $N = 10$ and $N = 32$ were housed in different sample holders in separate shields and thus did not share the same external coil and flux lines.

3. Device characterization

The flux-dependence of the SQUID array frequency is reported for both devices in Fig. 11. The value of the flux Φ_X is controlled by applying a direct current to the external coil. We convert the current applied to the flux threading the SQUIDs by fitting a larger flux modulation sweep over more than one period. The two devices are made of SQUIDs with identical junctions and have a similar total capacitance. As a consequence their maximum frequency differs due to the total number of SQUID N in the two arrays.

We observe an unexplained dip in the flux modulation of device $N = 32$ (blue). This feature is periodically

repeated for Φ_0 increments of the flux Φ_X , and we observe no hysteretic effect. This spurious dip was observed across several cooldowns at the same position. A similar device with $N = 46$ SQUIDs located on the same chip does not show a similar dip. Cross markers in Fig. 11 indicate the flux operating point of both devices, and the segment on the x-axes show the maximum flux modulation performed in this work. The $N = 32$ SQUID array is always operated far from the unexpected feature which thus does not impact the results of the experiment.

Because of the nonlinear flux dependence of the frequency of the resonators, the applied frequency modulation is not exactly sinusoidal, $\zeta \cos(\Omega t)$, as stated in the Hamiltonian Eq. (1). Moreover, for large modulation strength ζ , the frequency modulation is not symmetric around ω_{wp} . This results in a deviation of the LZSM resonances \bar{m} away from $\Delta_{\bar{m}}$. We observe this deviation in our measurements, most clearly in Fig. 4 where ζ is as large as 1.1 GHz. It is also apparent in Fig. 6 (d-f) where the data are systematically shifted to negative frequencies compared to the superimposed numerical simulations. The deviation from the LZ mode position expected for an ideal modulation is towards negative detuning because of the curvature of the flux dependence of the frequency. The deviation increases when the flux operating point is brought closer to zero flux where the curvature is more important. This phenomenon is reported and explained in Ref. [71].

From the measurement of the room-temperature normal-state resistance, we estimate the single junction Josephson energy to $E_J/h \approx 170$ GHz. The frequencies and Kerr non-linearities of the SQUID array modes can

be simulated using a lumped-model and assuming $E_J \gg E_C$ [44]. From this model, we estimate the plasma frequency of the junctions to $\hbar\omega_P = \sqrt{8E_J E_C} \approx h \times 39$ GHz. The zero-flux frequency of the Kerr $N = 10$ device is out of our measurement bandwidth of 4-8 GHz, but we estimate it to be approximately 13 GHz from the lumped model discussed above. We find a single junction charging energy $E_C = e^2/2C_J \approx h \times 1.1$ GHz. Even for the flux operating point $\Phi_X/\Phi_0 \approx 0.455$ of the $N = 10$ device, the effective Josephson energy of the SQUID remains much larger than the charging energy, ensuring the validity of the Kerr approximation of the Josephson Hamiltonian.

We then carefully characterize the two devices at their chosen flux operating points. The parameters of the devices, reported in Table I, are obtained by fitting S_{21} without modulating the frequency. The SQUID array is modeled as a Kerr resonator according to the Hamiltonian of Eq. (1) with $\zeta = 0$. First we fit the transmission at low enough power to ensure an average occupation of less than one photon. This allows us to neglect the Kerr nonlinearity and the dephasing. The expression of the linear transmission coefficient S_{21} is obtained from standard notch configuration input-output theory [36, 72] as

$$S_{21} = 1 - \frac{\kappa_{\text{ext}}}{\kappa_{\text{ext}} + \kappa_{\text{int}} + 2i\Delta} \times \frac{e^{i\phi}}{\cos\phi}. \quad (\text{B1})$$

Following the diameter correction method [73], we add the last term to compensate for impedance mismatch. To fit the measured transmissions to this expression, we first normalize the data by a background transmission measured with the SQUID threaded by a different flux, such that its frequency lies outside of the measurement range. All experimental data reported in this work are normalized this way. We then extract the precise operating frequency as well as the internal and external loss rates of each device.

To determine the Kerr nonlinearity χ and the dephasing rate κ_ϕ , we need to fit the power dependence of the transmission which is reported in Fig. 2. A simple analytical model can be used for weakly anharmonic devices satisfying $|\chi| \ll \kappa$ [36, 74]. Instead we directly solve the Lindblad master equation [Eq. (2)] to find the intracavity field α , again setting $\zeta = 0$ in the Hamiltonian. This model is valid for both devices studied in this work and accounts for dephasing. Using input-output theory, we convert α to the transmission scattering parameter using the following relation

$$S_{21} = 1 - i \frac{\kappa_{\text{ext}} \alpha}{2F}. \quad (\text{B2})$$

The drive amplitude F is related to the input power P_{in} as

$$F = \sqrt{\frac{P_{\text{in}} \kappa_{\text{ext}}}{\hbar\omega_d}}. \quad (\text{B3})$$

We start by fitting the device $N = 10$ in the Kerr regime. We perform a global simultaneous fit of approximately ten frequency sweeps at different driving powers. We use the parameters obtained from the low-power

fit and keep three independent fitting parameters: κ_ϕ , χ , and the attenuation of the input drive line. Because single multiphoton transitions are well-resolved with the Kerr device, we can obtain all three parameters without prior calibration of the input attenuation. The Kerr multiphoton resonances reported in Fig. 2 (c-e) are not equispaced by χ , instead the spacing increases for larger $|n\rangle$. We attribute this effect to non-negligible higher-order nonlinearities from the expansion of the Josephson cosine potential. To accurately reproduce the experimental data of the $N = 10$ device, we also include a term of the form $\chi^{(5)}(\hat{a}^\dagger)^3\hat{a}^3$ in the model, and find a value of $\chi^{(5)} \approx 5\%\chi$ [47].

Finding the Kerr nonlinearity of the Duffing device, however, requires knowing the input attenuation. But the feedline of the Kerr and Duffing devices are connected on the same microwave switch, as depicted in Fig. 10. Therefore we assume that the input attenuation obtained from the fit of the Kerr device is also valid for the Duffing device. We perform a similar global fit of the power dependence of the transmission of the Duffing device, this time with only two free fitting parameters: χ and κ_ϕ . Simulations of the Kerr shift of both devices are shown in Fig. 2.

Appendix C: Additional data

In this section, we report additional measurements performed with the $N = 32$ Duffing device in the linear regime. In Fig. 12 we repeat the linear regime LZSM interferometry measurements of Fig. 3(d-f) for different values of Ω and ζ . The drive power is set to the same low value as in Fig. 3 to remain in the linear regime with a low photon occupation number. In panels (a-d), we sweep the modulation strength ζ for increasing values of modulation frequency Ω . LZSM resonances are visible for $\zeta \geq |\Delta|$, irrespective of the value of Ω . As expected from Eq. (3), the spacing between LZSM resonances is equal to Ω . In panels (e-h), we sweep the modulation frequency Ω for increasing modulation strengths ζ . We observe more and more LZSM resonances as ζ is increased, and again the extension of the resonances is approximately confined to $|\Delta| < \zeta$. These measurements highlight the superb control offered by the platform on the position and number of modes, as for instance in panel (a) we observe clearly LZSM resonances up to mode $\bar{m} = 25$.

Next, in Fig. 13 we repeat the Duffing regime LZSM interferometry of Fig. 6, but this time sweeping the modulation frequency Ω at fixed ζ . We repeat this measurement for three increasing values of drive power P_{in} . For the lowest drive shown in panel (a), individual LZSM resonances remain mostly isolated. However, when compared to the linear regime of weak drive, LZSM resonances appear distorted with a rounded shape. This rounding is a combination of the Kerr nonlinearity bending the peak to negative frequencies, and the modulation of the effective drives $F_{\bar{m}}$ that controls the peak bendings.

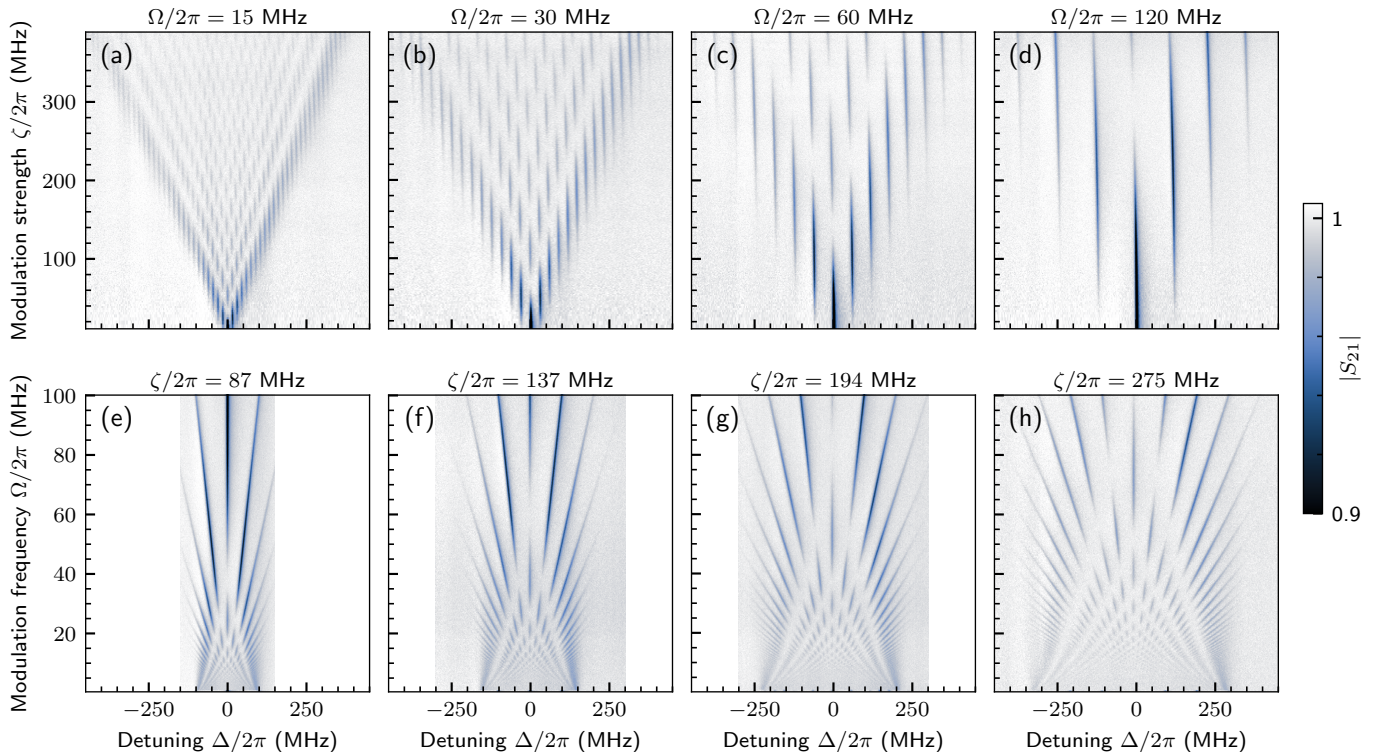


FIG. 12. Extended data of LZSM interference patterns in the linear regime. The measurements are performed on the device $N = 32$ with the same weak drive power as in Fig. 3 (d-f). In panels (a-d), the same sweep of modulation strength ζ is repeated for increasing modulation frequencies Ω . In panels (e-h), the same sweep of modulation frequency Ω is repeated for increasing modulation strengths ζ . These measurements highlight the exquisite control over both the frequency spacing and the number of resonances offered by the platform, with for instance LZSM resonances up to $m = \pm 25$ visible in (a).

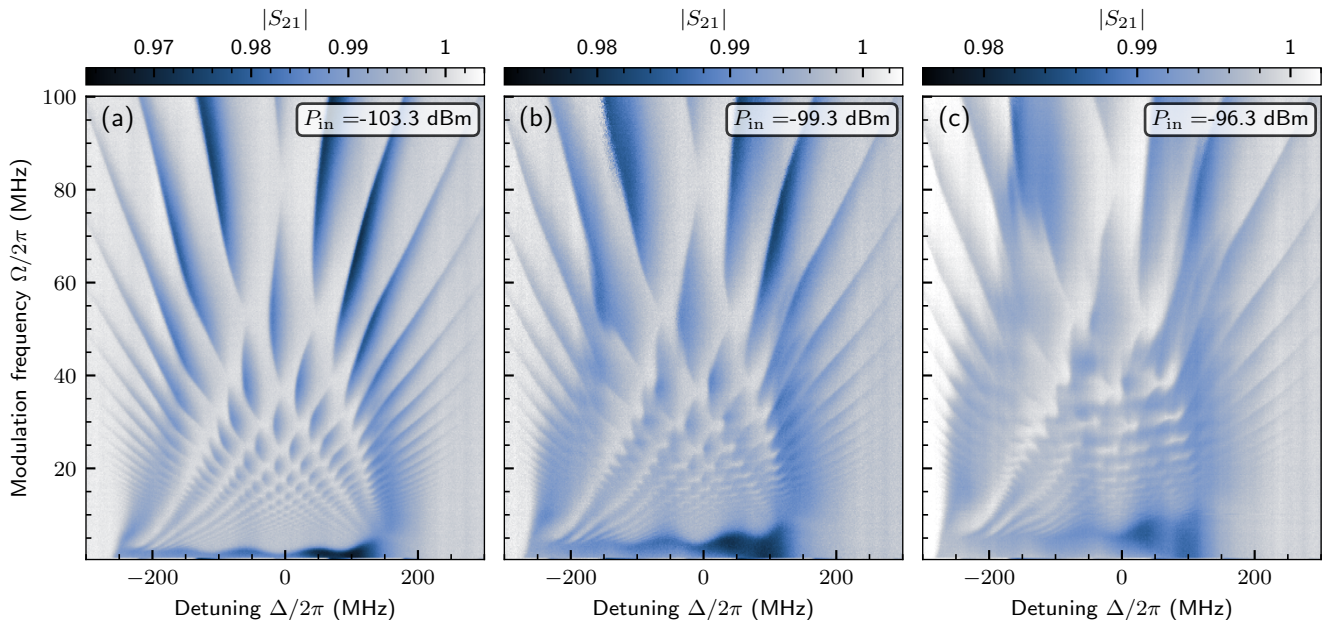


FIG. 13. Extended data of LZSM interferometry in the Duffing regime measured with the $N = 32$ device. The magnitude of S_{21} is measured versus Δ and Ω for increasing drive power P_{in} . The modulation strength is fixed to $\zeta/2\pi = 206$ MHz.

For increasing drive power, as shown in panels (b) and (c), the interference pattern gets more distorted and individual resonances start merging together. In this regime, the effective model of Eq. (3) is no longer valid and a

full Floquet-Lindblad treatment is required. As we have theoretically shown, the broadening and distortion of the LZSM interference pattern in the Duffing regime is associated to a dissipative quantum chaotic phase.

-
- [1] Alexandre Blais, Arne L. Grimsmo, S. M. Girvin, and Andreas Wallraff, “Circuit quantum electrodynamics,” *Rev. Mod. Phys.* **93**, 025005 (2021).
- [2] Ehud Altman, Kenneth R. Brown, Giuseppe Carleo, Lincoln D. Carr, Eugene Demler, Cheng Chin, Brian DeMarco, Sophia E. Economou, Mark A. Eriksson, Kai-Mei C. Fu, Markus Greiner, Kaden R.A. Hazzard, Randall G. Hulet, Alicia J. Kollár, Benjamin L. Lev, Mikhail D. Lukin, Ruichao Ma, Xiao Mi, Shashank Misra, Christopher Monroe, Kater Murch, Zaira Nazario, Kang-Kuen Ni, Andrew C. Potter, Pedram Roushan, Mark Saffman, Monika Schleier-Smith, Irfan Siddiqi, Raymond Simmonds, Meenakshi Singh, I.B. Spielman, Kristan Temme, David S. Weiss, Jelena Vučković, Vladan Vuletić, Jun Ye, and Martin Zwierlein, “Quantum simulators: Architectures and opportunities,” *PRX Quantum* **2**, 017003 (2021).
- [3] Lev Landau, “Zur theorie der energieübertragung. ii,” *Physikalische Zeitschrift der Sowjetunion* **2**, 46 (1932).
- [4] Clarence Zener, “Non-adiabatic crossing of energy levels,” *Proceedings of the Royal Society of London. Series A, Containing Papers of a Mathematical and Physical Character* **137**, 696–702 (1932).
- [5] ECG Stückelberg, “Theorie der unelastischen stösse zwischen atomen,” *Helv. Phys. Acta* **5**, 369 (1932).
- [6] Ettore Majorana, “Atomi orientati in campo magnetico variabile,” *Il Nuovo Cimento (1924-1942)* **9**, 43–50 (1932).
- [7] Oleh V. Ivakhnenko, Sergey N. Shevchenko, and Franco Nori, “Nonadiabatic landau–zener–stückelberg–majorana transitions, dynamics, and interference,” *Physics Reports* **995**, 1–89 (2023).
- [8] William D. Oliver, Yang Yu, Janice C. Lee, Karl K. Berggren, Leonid S. Levitov, and Terry P. Orlando, “Mach-Zehnder interferometry in a strongly driven superconducting qubit,” *Science* **310**, 1653–1657 (2005).
- [9] Mika Sillanpää, Teijo Lehtinen, Antti Paila, Yuriy Makhlin, and Pertti Hakonen, “Continuous-Time Monitoring of Landau-Zener Interference in a Cooper-Pair Box,” *Physical Review Letters* **96**, 187002 (2006).
- [10] J. Stehlik, Y. Dovzhenko, J. R. Petta, J. R. Johansson, F. Nori, H. Lu, and A. C. Gossard, “Landau-Zener-Stückelberg interferometry of a single electron charge qubit,” *Physical Review B* **86**, 121303 (2012).
- [11] F. Forster, G. Petersen, S. Manus, P. Hänggi, D. Schuh, W. Wegscheider, S. Kohler, and S. Ludwig, “Characterization of Qubit Dephasing by Landau-Zener-Stückelberg-Majorana Interferometry,” *Physical Review Letters* **112**, 116803 (2014).
- [12] Lilian Childress and Jean McIntyre, “Multifrequency spin resonance in diamond,” *Physical Review A* **82**, 033839 (2010).
- [13] David Niepce, Jonathan J. Burnett, Marina Kudra, Jared H. Cole, and Jonas Bylander, “Stability of superconducting resonators: Motional narrowing and the role of Landau-Zener driving of two-level defects,” *Science Advances* **7** (2021), 10.1126/sciadv.abh0462.
- [14] E. Dupont-Ferrier, B. Roche, B. Voisin, X. Jehl, R. Wacquez, M. Vinet, M. Sanquer, and S. De Franceschi, “Coherent Coupling of Two Dopants in a Silicon Nanowire Probed by Landau-Zener-Stückelberg Interferometry,” *Physical Review Letters* **110**, 136802 (2013).
- [15] Jiangbo He, Dong Pan, Mingli Liu, Zhaozheng Lyu, Zhongmou Jia, Guang Yang, Shang Zhu, Guangtong Liu, Jie Shen, Sergey N. Shevchenko, Franco Nori, Jianhua Zhao, Li Lu, and Fanning Qu, “Quantifying quantum coherence of multiple-charge states in tunable Josephson junctions,” *npj Quantum Information* **10**, 1–8 (2024).
- [16] Gang Cao, Hai-Ou Li, Tao Tu, Li Wang, Cheng Zhou, Ming Xiao, Guang-Can Guo, Hong-Wen Jiang, and Guo-Ping Guo, “Ultrafast universal quantum control of a quantum-dot charge qubit using Landau-Zener-Stückelberg interference,” *Nature Communications* **4**, 1401 (2013).
- [17] Anasua Chatterjee, Sergey N. Shevchenko, Sylvain Barraud, Rubén M. Otxoa, Franco Nori, John J. L. Morton, and M. Fernando Gonzalez-Zalba, “A silicon-based single-electron interferometer coupled to a fermionic sea,” *Physical Review B* **97**, 045405 (2018).
- [18] Mikael Kervinen, Jhon E. Ramírez-Muñoz, Alpo Välimaa, and Mika A. Sillanpää, “Landau-Zener-Stückelberg Interference in a Multimode Electromechanical System in the Quantum Regime,” *Physical Review Letters* **123**, 240401 (2019).
- [19] P. Y. Wen, O. V. Ivakhnenko, M. A. Nakonechnyi, B. Suri, J.-J. Lin, W.-J. Lin, J. C. Chen, S. N. Shevchenko, Franco Nori, and I.-C. Hoi, “Landau-Zener-Stückelberg-Majorana interferometry of a superconducting qubit in front of a mirror,” *Physical Review B* **102**, 075448 (2020).
- [20] Yu-Han Chang, Dmytro Dubyna, Wei-Chen Chien, Chien-Han Chen, Cen-Shawn Wu, and Watson Kuo, “Circuit quantum electrodynamics with dressed states of a superconducting artificial atom,” *Scientific Reports* **12**, 22308 (2022).
- [21] Jonas Lidal and Jeroen Danon, “Generation of Schrödinger-cat states through photon-assisted Landau-Zener-Stückelberg interferometry,” *Physical Review A* **102**, 043717 (2020).
- [22] Lu Wang, Fulu Zheng, Jiaming Wang, Frank Großmann, and Yang Zhao, “Schrödinger-Cat States in Landau-Zener-Stückelberg-Majorana Interferometry: A Multiple Davydov Ansatz Approach,” *The Journal of Physical Chemistry B* **125**, 3184–3196 (2021).
- [23] O. V. Ivakhnenko, S. N. Shevchenko, and Franco Nori, “Simulating quantum dynamical phenomena using classical oscillators: Landau-Zener-Stückelberg-Majorana interferometry, latching modulation, and motional averaging,” *Scientific Reports* **8**, 12218 (2018).
- [24] Xin Zhou, Chun Zhao, Dingbang Xiao, Jiangkun Sun, Guillermo Sobreviela, Dustin D. Gerrard, Yunhan Chen,

- Ian Flader, Thomas W. Kenny, Xuezhong Wu, and Ashwin A. Seshia, “Dynamic modulation of modal coupling in microelectromechanical gyroscopic ring resonators,” *Nature Communications* **10**, 4980 (2019).
- [25] Heribert Lorenz, Sigmund Kohler, Anton Parafilo, Mikhail Kiselev, and Stefan Ludwig, “Classical analogue to driven quantum bits based on macroscopic pendula,” *Scientific Reports* **13**, 18386 (2023).
- [26] Lorenzo Bernazzani and Guido Burkard, “Fluctuating parametric drive of coupled classical oscillators can simulate dissipative qubits,” *Physical Review Research* **6**, 013284 (2024).
- [27] Iacopo Carusotto, Andrew A. Houck, Alicia J. Kollár, Pedram Roushan, David I. Schuster, and Jonathan Simon, “Photonic materials in circuit quantum electrodynamics,” *Nature Physics* **16**, 268–279 (2020).
- [28] Iacopo Carusotto and Cristiano Ciuti, “Quantum fluids of light,” *Rev. Mod. Phys.* **85**, 299–366 (2013).
- [29] J. S. Huber, G. Rastelli, M. J. Seitner, J. Kölbl, W. Belzig, M. I. Dykman, and E. M. Weig, “Spectral evidence of squeezing of a weakly damped driven nanomechanical mode,” *Phys. Rev. X* **10**, 021066 (2020).
- [30] Shiqian Ding, Gleb Maslennikov, Roland Hablützel, and Dzmitry Matsukevich, “Cross-Kerr nonlinearity for phonon counting,” *Phys. Rev. Lett.* **119**, 193602 (2017).
- [31] T. Yamaji, S. Kagami, A. Yamaguchi, T. Satoh, K. Koshino, H. Goto, Z. R. Lin, Y. Nakamura, and T. Yamamoto, “Spectroscopic observation of the crossover from a classical Duffing oscillator to a Kerr parametric oscillator,” *Phys. Rev. A* **105**, 023519 (2022).
- [32] Patrick Winkel, Kiril Borisov, Lukas Grünhaupt, Dennis Rieger, Martin Speieger, Francesco Valenti, Alexey V. Ustinov, Wolfgang Wernsdorfer, and Ioan M. Pop, “Implementation of a transmon qubit using superconducting granular aluminum,” *Phys. Rev. X* **10**, 031032 (2020).
- [33] Note that here multiphoton resonance refers to the fact that absorbing n photons leads to the n th excited state of the resonator. This is not the multiphoton Rabi resonance, where n driving photons are absorbed to populate the excited level of the qubit.
- [34] Mark I. Dykman, *Fluctuating Nonlinear Oscillators: From Nanomechanics to Quantum Superconducting Circuits* (Oxford University Press, 2012).
- [35] Qi-Ming Chen, Michael Fischer, Yuki Nojiri, Michael Renger, Edwar Xie, Matti Partanen, Stefan Pogorzalek, Kirill G. Fedorov, Achim Marx, Frank Deppe, and Rudolf Gross, “Quantum behavior of the Duffing oscillator at the dissipative phase transition,” *Nature Communications* **14** (2023), 10.1038/s41467-023-38217-x.
- [36] Guillaume Beaulieu, Fabrizio Minganti, Simone Frasca, Vincenzo Savona, Simone Felicetti, Roberto Di Candia, and Pasquale Scarlino, “Observation of first- and second-order dissipative phase transitions in a two-photon driven Kerr resonator,” (2023), 10.48550/ARXIV.2310.13636.
- [37] M. Foss-Feig, P. Niroula, J. T. Young, M. Hafezi, A. V. Gorshkov, R. M. Wilson, and M. F. Maghrebi, “Emergent equilibrium in many-body optical bistability,” *Physical Review A* **95**, 043826 (2017).
- [38] Filippo Vicentini, Fabrizio Minganti, Riccardo Rota, Giuliano Orso, and Cristiano Ciuti, “Critical slowing down in driven-dissipative Bose-Hubbard lattices,” *Phys. Rev. A* **97**, 013853 (2018).
- [39] Zejian Li, Ferdinand Claude, Thomas Boulier, Elisabeth Giacobino, Quentin Glorieux, Alberto Bramati, and Cristiano Ciuti, “Dissipative phase transition with driving-controlled spatial dimension and diffusive boundary conditions,” *Phys. Rev. Lett.* **128**, 093601 (2022).
- [40] Filippo Ferrari, Luca Gravina, Debbie Eeltink, Pasquale Scarlino, Vincenzo Savona, and Fabrizio Minganti, “Steady-state quantum chaos in open quantum systems,” (2023), 10.48550/ARXIV.2305.15479.
- [41] Daniel Dahan, Geva Arwas, and Eytan Grosfeld, “Classical and quantum chaos in chirally-driven, dissipative Bose-Hubbard systems,” *npj Quantum Information* **8** (2022), 10.1038/s41534-022-00518-2.
- [42] Joachim Cohen, Alexandru Petrescu, Ross Shillito, and Alexandre Blais, “Reminiscence of classical chaos in driven transmons,” *PRX Quantum* **4**, 020312 (2023).
- [43] Nicholas A. Masluk, Ioan M. Pop, Archana Kamal, Zlatko K. Mineev, and Michel H. Devoret, “Microwave Characterization of Josephson Junction Arrays: Implementing a Low Loss Superinductance,” *Physical Review Letters* **109**, 137002 (2012).
- [44] T. Weißl, B. Küng, E. Dumur, A. K. Feofanov, I. Matei, C. Naud, O. Buisson, F. W. J. Hekking, and W. Guichard, “Kerr coefficients of plasma resonances in Josephson junction chains,” *Physical Review B* **92**, 104508 (2015).
- [45] Yu. Krupko, V. D. Nguyen, T. Weißl, É. Dumur, J. Puer-tas, R. Dassonneville, C. Naud, F. W. J. Hekking, D. M. Basko, O. Buisson, N. Roch, and W. Hasch-Guichard, “Kerr nonlinearity in a superconducting Josephson meta-material,” *Physical Review B* **98**, 094516 (2018).
- [46] Daniel A. Lidar, “Lecture notes on the theory of open quantum systems,” (2019), 10.48550/ARXIV.1902.00967.
- [47] The resonator exhibits deviation from the pure Kerr nonlinearity prediction due to non-negligible effects of higher nonlinearities, e.g., terms of the form $\chi^{(5)}(\hat{a}^\dagger)^3\hat{a}^3$. We estimate $\chi^{(5)}/2\pi \approx -1.1 \text{ MHz} \approx 5\% \chi/2\pi$. As such, although the $\chi^{(5)}$ term produces small changes compared to the model in Eq. (1), all the relevant physical features of the LZSM interference are captured by the Kerr model. We also note additional nonlinear effects due to the large values of flux modulation used to obtain the wanted ζ .
- [48] One shows that, assuming at most two-photon in the system, the maximum of the two-photon population occurs at multiphoton resonance $\Delta = \chi$, where
- $$\langle 2 | \hat{\rho}_{\text{ss}} | 2 \rangle = \frac{2F^4}{9F^4 + 2\kappa^2 [2(\kappa^2 + \chi^2) - 5F^2]} \simeq \frac{F^4}{2\kappa^2\chi^2}.$$
- It follows that $F^2 \ll |\chi|\kappa$ ensures the validity of the qubit approximation.
- [49] To justify this approximation, consider the semiclassical (coherent state approximation) $\hat{\rho}_{\text{ss}} = |\alpha\rangle\langle\alpha|$. One finds that the photon number $n = |\alpha|^2$ satisfies
- $$\left[\frac{\kappa^2}{4} + (\Delta + n\chi)^2 \right] n - F^2 \simeq 2\Delta n^2 \chi + n \left(\Delta^2 + \frac{\kappa^2}{4} \right) - F^2 = 0.$$
- The solution to this equation can be expanded in powers of χ as
- $$n = n_0 \left(1 - n_0 \frac{8\Delta\chi}{4\Delta^2 + \kappa^2} \right), \quad \text{with } n_0 = \frac{F^2}{\Delta^2 + \kappa^2/4}.$$

The deviation from the linear regime $\delta n = 1 - n/n_0$ is then maximal for $\Delta = \kappa/(2\sqrt{3})$, and leading to

$$\delta n = \frac{3\sqrt{3}F^2\chi}{\kappa^3}.$$

As we are interested in $\delta n \ll 1$, we find back the formula in the main text.

- [50] Alexandre Le Boité, *Strongly correlated photons in arrays of nonlinear cavities*, *Theses*, Université Paris Diderot - Paris 7 (2015).
- [51] Rainer Grobe, Fritz Haake, and Hans-Jürgen Sommers, “Quantum Distinction of Regular and Chaotic Dissipative Motion,” *Physical Review Letters* **61**, 1899–1902 (1988).
- [52] A. Lemmer, C. Cormick, D. Tamascelli, T. Schaetz, S. F. Huelga, and M. B. Plenio, “A trapped-ion simulator for spin-boson models with structured environments,” *New Journal of Physics* **20**, 073002 (2018).
- [53] D. L. Underwood, W. E. Shanks, Jens Koch, and A. A. Houck, “Low-disorder microwave cavity lattices for quantum simulation with photons,” *Physical Review A* **86**, 023837 (2012).
- [54] G. P. Fedorov, S. V. Remizov, D. S. Shapiro, W. V. Pogosov, E. Egorova, I. Tsitsilin, M. Andronik, A. A. Dobronosova, I. A. Rodionov, O. V. Astafiev, and A. V. Ustinov, “Photon Transport in a Bose-Hubbard Chain of Superconducting Artificial Atoms,” *Physical Review Letters* **126**, 180503 (2021).
- [55] Vincent Jouanny, Simone Frasca, Vera Jo Weibel, Leo Peyruchat, Marco Scigliuzzo, Fabian Oppliger, Franco De Palma, Davide Sbroggio, Guillaume Beaulieu, Oded Zilberberg, and Pasquale Scarlino, “Band engineering and study of disorder using topology in compact high kinetic inductance cavity arrays,” (2024), 10.48550/arXiv.2403.18150, 2403.18150 [cond-mat, physics:quant-ph].
- [56] Anton Frisk Kockum, Adam Miranowicz, Simone De Liberato, Salvatore Savasta, and Franco Nori, “Ultrastrong coupling between light and matter,” *Nature Reviews Physics* **1**, 19–40 (2019).
- [57] Mariano Bonifacio, Daniel Domínguez, and María José Sánchez, “Landau-Zener-Stückelberg interferometry in dissipative circuit quantum electrodynamics,” *Physical Review B* **101**, 245415 (2020).
- [58] Raphaël Lescanne, Marius Villiers, Théau Peronnin, Alain Sarlette, Matthieu Delbecq, Benjamin Huard, Takis Kontos, Mazyar Mirrahimi, and Zaki Leghtas, “Exponential suppression of bit-flips in a qubit encoded in an oscillator,” *Nature Physics* **16**, 509–513 (2020).
- [59] Bogdan Damski, “The simplest quantum model supporting the kibble-zurek mechanism of topological defect production: Landau-zener transitions from a new perspective,” *Phys. Rev. Lett.* **95**, 035701 (2005).
- [60] Santiago Higuera-Quintero, Ferney J. Rodríguez, Luis Quiroga, and Fernando J. Gómez-Ruiz, “Experimental validation of the Kibble-Zurek mechanism on a digital quantum computer,” *Frontiers in Quantum Science and Technology* **1** (2022), 10.3389/frqst.2022.1026025.
- [61] M. Maragkou, C. Sánchez-Muñoz, S. Lazić, E. Chernysheva, H. P. van der Meulen, A. González-Tudela, C. Tejedor, L. J. Martínez, I. Prieto, P. A. Postigo, and J. M. Calleja, “Bichromatic dressing of a quantum dot detected by a remote second quantum dot,” *Phys. Rev. B* **88**, 075309 (2013).
- [62] Vincenzo Macrì, Alberto Mercurio, Franco Nori, Salvatore Savasta, and Carlos Sánchez Muñoz, “Spontaneous scattering of raman photons from cavity-qed systems in the ultrastrong coupling regime,” *Phys. Rev. Lett.* **129**, 273602 (2022).
- [63] Fabrizio Minganti and Dolf Huybrechts, “Arnoldi-lindblad time evolution: Faster-than-the-clock algorithm for the spectrum of time-independent and floquet open quantum systems,” *Quantum* **6**, 649 (2022).
- [64] H. Markum, R. Pullirsch, and T. Wettig, “Non-Hermitian Random Matrix Theory and Lattice QCD with Chemical Potential,” *Physical Review Letters* **83**, 484–487 (1999).
- [65] Gernot Akemann, Mario Kieburg, Adam Mielke, and Tomaz Prosen, “Universal Signature from Integrability to Chaos in Dissipative Open Quantum Systems,” *Physical Review Letters* **123**, 254101 (2019).
- [66] Lucas Sá, Pedro Ribeiro, and Tomaz Prosen, “Complex Spacing Ratios: A Signature of Dissipative Quantum Chaos,” *Physical Review X* **10**, 021019 (2020).
- [67] We set the cutoff $c_{\min} = \bar{C}/1000$ where \bar{C} is the average of the spectral weights in Eq. (A18), as detailed in Ref. [40]. For the Floquet Liouvillian, we found that some of the $|c_j|$ were very large (order of magnitudes bigger than one). As the average procedure of the spectral weights would have been affected by those outliers, we restrict the mean to the ones such that $|c_j| \leq 1$. Such a choice is justified as a spectral coefficient $|c_j| > 1$ will be for sure chosen with the SSQT protocol, and we get a meaningful c_{\min} as in Ref. [40].
- [68] D.F. Walls and Gerard J. Milburn, eds., *Quantum Optics* (Springer Berlin Heidelberg, Berlin, Heidelberg, 2008).
- [69] Howard M. Wiseman and Gerard J. Milburn, *Quantum Measurement and Control*, 1st ed. (Cambridge University Press, 2009).
- [70] J M Kreikebaum, K P O’Brien, A Morvan, and I Siddiqi, “Improving wafer-scale Josephson junction resistance variation in superconducting quantum coherent circuits,” *Superconductor Science and Technology* **33**, 06LT02 (2020).
- [71] Tong Wu, Yuxuan Zhou, Yuan Xu, Song Liu, and Jian Li, “Landau-Zener-Stückelberg Interference in Nonlinear Regime,” *Chinese Physics Letters* **36**, 124204 (2019).
- [72] Qi-Ming Chen, Matti Partanen, Florian Fesquet, Kedar E. Honasoge, Fabian Kronowetter, Yuki Nojiri, Michael Renger, Kirill G. Fedorov, Achim Marx, Frank Deppe, and Rudolf Gross, “Scattering coefficients of superconducting microwave resonators. II. System-bath approach,” *Physical Review B* **106**, 214506 (2022).
- [73] M. S. Khalil, M. J. A. Stoutimore, F. C. Wellstood, and K. D. Osborn, “An analysis method for asymmetric resonator transmission applied to superconducting devices,” *Journal of Applied Physics* **111**, 054510 (2012).
- [74] Christopher Eichler and Andreas Wallraff, “Controlling the dynamic range of a Josephson parametric amplifier,” *EPJ Quantum Technology* **1**, 1–19 (2014).